České vysoké učení technické v Praze
Fakulta jaderná a fyzikálně inženýrská

Diplomová práce

Studium mezonu J/ψ v experimentu STAR

Praha, 2011

Autor: Bc. Olga Hájková

Vedoucí práce: Mgr. Jaroslav Bielčík, Ph.D.

Czech Technical University in Prague
Faculty of Nuclear Sciences and Physical Engineering

Diploma thesis

Study of J/ψ in STAR experiment

Prague, 2011

Author: Bc. Olga Hájková

Supervisor: Mgr. Jaroslav Bielčík, Ph.D.

Prohlášení

Prohlašuji, že jsem svou diplomovou práci vypracovala samostatně a použila jsem pouze podklady (literaturu, projekty, SW atd.) uvedené v přiloženém seznamu.

Nemám závažný důvod proti užití tohoto školního díla ve smyslu § 60 Zákona č.121/2000 Sb., o právu autorském, o právech souvisejících s právem autorským a o změně některých zákonů (autorský zákon).

V Praze dne ________________ ________________________
podpis

Study of J/ψ in STAR experiment

Author: Bc. Olga Hájková

Field of Study: Nuclear Engineering

Specialization: Experimental Nuclear Physics

Supervisor: Mgr. Jaroslav Bielčík, Ph.D.

Abstract:

Since the J/ψ production in QGP is expected to be suppressed due to color screening, the suppression of the J/ψ yield is considered as the most promising signature of the QGP formation. Such a high temperature and high density state is supposed to have been realized in the early universe and can be produced in central nucleus-nucleus collisions at high energy. The J/ψ productions in $d + Au$ collisions in the center of mass energy per nucleon-nucleon pair pair $\sqrt{s_{NN}} = 200$ GeV were studied at the STAR experiment at the Relativistic Heavy Ion Collider at the Brookhaven National Laboratory.

The J/ψ yield was obtained via di-electron decay channel, and after efficiency and acceptance corrections, the invariant yield was compared to the yield in $p+p$ collisions, and the nuclear modification factor was extracted to be $R^{J/\psi}_{d+Au} = 0.55 \pm 0.18$ $(0.48 \pm 0.06, 1.08 \pm 0.13)$ for the most central, semi-peripheral and peripheral collisions, respectively. Results are consistent with other published results from the STAR and the PHENIX experiments.

Keywords: charmonia, STAR, J/ψ meson, suppression, cold nuclear matter effects, nuclear modification factor

Studium mezonu J/ψ v experimentu STAR

Autor: Bc. Olga Hájková

Obor: Jaderné inženýrství

Specializace: Experimentální jaderná fyzika

Vedoucí práce: Mgr. Jaroslav Bielčík, Ph.D.

Abstrakt:

Produkce J/ψ mezonu je v kvark-gluonové plazmě potlačena z důvodu barevného odstínění, toto potlačení se považuje za nejvýznamnější známku vzniku QGP. Predpokládá se, že stav hmoty s takto vysokou hustotou energie a teplotou se vyskytoval v prvotní fázi vzniku vesmíru a v jádro-jaderných srážkách. Produkce J/ψ mezonu byla studována ve srážkách $d + Au$ při energii $\sqrt{s_{NN}} =$ 200 GeV na experimentu STAR v Brookhavenské národní laboratoři.

Signál J/ψ byl zrekonstruován z elektron-pozitronového rozpadového kanálu a výtěžek byl korigovaný s ohledem na akceptanci detektoru a účinnosti analýzy. Po srovnání korigovaneho spektra s výsledky získanými v $p + p$ srážkách byl spočítán jaderný modifikační faktor $R^{J/\psi}_{d+Au} = 0.55 \pm 0.18$ $(0.48 \pm 0.06, 1.08 \pm 0.13)$, pro centrální, semiperiferální a periferální srážky. Dosažené výsledky jsou konzistentní s výsledky publikovanými v kolaboracích STAR a PHENIX.

Klíčová slova: charmonia, STAR, J/ψ mezon, potlačení produkce, efekty chladné jaderné hmoty, jaderný modifikační faktor

Acknowledgements

I would like to express my gratitude to all those who gave me the possibility to complete this work. I am very grateful to my supervisor Jaroslav Bielčík for his invaluable help, advice and support during creation of this work. I am also very thankful to Christopher Powell, Jan Kapitán, Michal Zerola and David Tlustý for their important advices and helpful information. Last but not least I would like to thank to my father Vladimír Rogalewicz for languages consultations.

Contents

List of Figures

List of Tables

Introduction

The strongly interacting matter at sufficiently high density or temperature undergoes a phase transition from the hadronic matter to a new state, so-called quark gluon plasma (QGP), when quarks are no longer confined into color neutral bound states. QGP is believed to exist in the early universe, shortly after the Big Bang. Current experiments as RHIC or at LHC provide a possibility to produce QGP in a laboratory in nucleus-nucleus collisions and the experimental detection of QGP represents one of the greatest challenges of present high energy physics.

The cardinal question is what observable signatures can the predicted new form of the matter provide. One of the probes, proposed by Matsui and Satz [1], for searching for QGP and for investigating its properties is a study of the quarkonia production. It is predicted that due to the color screening the quarkonia production is suppressed when QGP is presented at sufficiently high temperature. Before resolving whether QGP was formed or not, it is necessary to study the production of J/ψ in hadron-hadron, hadron-ion and ion-ion collisions separately to distinguish cold nuclear matter effects from the suppression due to the formation of QGP. The STAR allows to study J/ψ meson in e^+e^- channel.

1 Heavy ion collisions

Quantum Chromodynamics (QCD) is a theory of strong interaction between quarks and gluons. Quarks carry a quantum number called color and they are confined by coloured gluons in colorless hadrons, mesons and baryons. There are three possible colors of quarks: red, blue, and green, and three possible anticolors of antiquarks. Gluons carry one color and one anticolor. Elementary particles of the matter and their features are shown in Tab. 1 and 2.

Quark	m [GeV]	Q	I	I_Z	S	C	B	T
u	0.0015 - 0.0033	$-\frac{1}{3}$	$\frac{1}{2}$	$-\frac{1}{2}$	0	0	0	0
d	0.0035 - 0.0060	$+\frac{2}{3}$	$\frac{1}{2}$	$+\frac{1}{2}$	0	0	0	0
s	$0.104^{+0.026}_{-0.034}$	$-\frac{1}{3}$	0	0	-1	0	0	0
c	$1.27^{+0.07}_{-0.11}$	$+\frac{2}{3}$	0	0	0	+1	0	0
b	$4.20^{+0.17}_{-0.07}$	$-\frac{1}{3}$	0	0	0	0	-1	0
t	171.2 ± 2.1	$+\frac{2}{3}$	0	0	0	0	0	+1

Table 1: Main properties of quarks, m is mass, Q is an electric charge, I is an isospin, I_Z is the 3rd component of an isospin, S is a strangeness, C is a charmness, B is a bottomness and T is a topness [2] [3].

Lepton	m [MeV]	Q	L_e	L_μ	L_τ
e	0.511	-1	+1	0	0
ν_e	$< 2.2 \cdot 10^{-6}$	0	+1	0	0
μ	105.65	-1	0	+1	0
ν_μ	< 0.17	0	0	+1	0
τ	1776.84	-1	0	0	+1
ν_τ	< 15.50	0	0	0	+1

Table 2: Main properties of leptons, m is mass, Q is a charge, L_e is an electron number, L_μ is a muon number, and L_τ is a tau number [2] [3].

The interaction between two coloured particles is characterized by the strong interaction coupling constant α_s and by the potential V:

$$\alpha_s = \frac{12\pi}{(33 - 2N_f)\ln(\frac{Q^2}{\lambda_{QCD}})}, \tag{1}$$

$$V = \sigma r - \frac{4\alpha_s}{3r}, \tag{2}$$

where Q^2 is the four-momentum transfer, N_f is the number of quark flavors, λ_{QCD} is the typical QCD scale ($\lambda_{QCD} \sim 0.2$GeV), r is the distance between quarks, and σ is the string constant.

The coupling constant α_s for the strong force becomes smaller at shorter distances. This effect is known as asymptotic freedom. Another important property of strong interaction is the color confinement. The confinement means that the interaction between quarks is growing at larger distances, and quarks are prevented to become free. The coupling constant α_s decreases with an increase in the momentum transfer and decreases in the environment of high temperature and/or densities [4]. When the system reaches the critical temperature, the color confinement is broken and matter passes through phase transition from the confined nuclear matter to the deconfined state. This is predicted from calculations on lattice QCD. This method uses finite space-time lattice points on a grid to numerically compute thermodynamic properties [5] [6]. A phase diagram of hadronic matter is shown in Fig. 1 as a function of temperature and the baryon density. The assumed phase transition line between hadron gas and quark gluon plasma (QGP) is denoted.

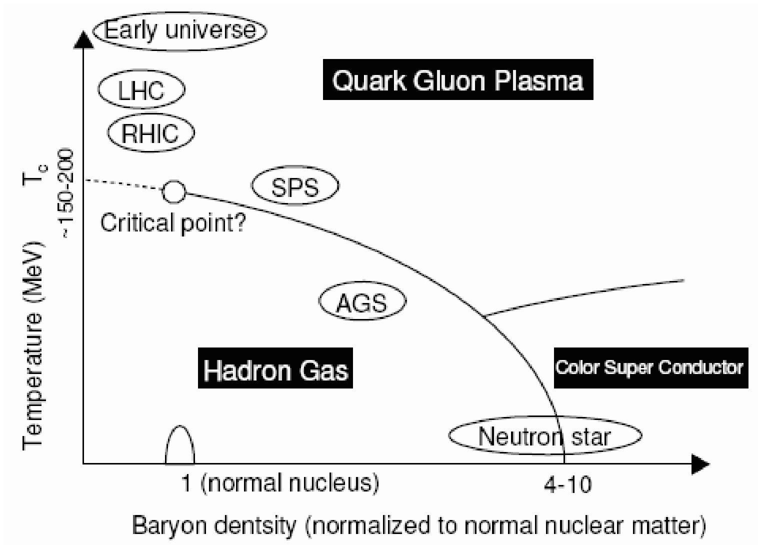

Figure 1: A phase diagram of matter. Assumed phase transition lines are denoted [7].

1.1 QGP and its signatures

Quark gluon plasma is a new state of matter which is composed of deconfined quarks and gluons. QGP is believed to exist in the early universe, about 10^{-6} second after the Big Bang. High energy heavy ion collisions provide a possibility to produce QGP in a laboratory. Current calculations show that the transition happens around the critical temperature T_c = 150 - 180 MeV, which corresponds to the energy density of about 0.3 - 1.0 GeV/fm^3 [8].

Even if QGP is produced in a laboratory, its identification is difficult because of its very short lifetime. Its impossible to directly observe its thermodynamics properties. So, its necessary to rely on indirect measurements of QGP formation. Certain signatures of the phase transition could allow us to establish whether the matter is deconfined or not. Observable signatures in high energy heavy ion collisions could be divided into three classes: hard, electromagnetic and soft probes. Hard probes that include J/ψ suppression are of the most interest of this work.

As mentioned above also the J/ψ suppression research has been considered as one of the most promising signatures for QGP formation since Matsui and Satz proposed it [1]. Due to color screening of the surrounding nuclear matter, J/ψ are expected to disassociate under certain conditions. Therefore, J/ψ has been used as a tool of searching for QGP formation in heavy ion collisions

1.2 Heavy ion collisions

High-energy heavy ion collisions at sufficient high energy are a powerful tool in the laboratory to realize conditions of possible the phase transition from ordinary nuclear matter to a deconfined quarks and gluons. When heavy ions collide together, the partons in the overlapping region of the colliding nuclei undergo inelastic collisions and transfer of their kinetic energy into the matter and transverse energy, which was discussed in detail by Bjorken [9]. The collision geometry, the nuclear modification factor, and the space-time evolution of heavy ion collisions are discussed briefly in Chapters 1.2.1, 1.2.2 and 1.2.3 respectively.

1.2.1 Collision geometry

As shown in Fig. 2, nucleons in collision can be classified into two groups, spectators and participants. Due to the relativistic effects nuclei are Lorentz contracted. The nucleons in the overlap region participate in the collision, so they are called participants. Nucleons in the other nucleus region are called spectators. The main parameter of colliding nuclei that quantifies the size of the participant group is the impact parameter b, the distance between trajectories of centers of two colliding nuclei. This way, we can speak about central and peripheral collisions. Low b indicates a central collision, and high b a peripheral one. Since the impact parameter and the number of the participant nucleons, N_{part}, cannot be measured directly, the observed particle multiplicity is used as an indirect measure of centrality. The relation between particle multiplicity, the number of participants, and the number of binary collisions, N_{coll}, can be calculated from the Glauber model [10].

There are two different Glauber calculations, optical and Monte Carlo. The Monte Carlo method is used for establishing N_{part} and N_{coll} in this analysis, as mentioned in Chapter 7.

Finally, centrality classes are determined by dividing the event multiplicity distribution into required bins. In the case of this analysis centrality classes

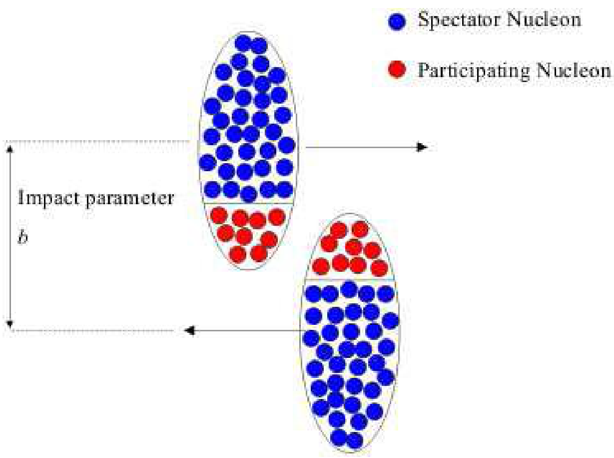

Figure 2: Spectators and participants of colliding nuclei [11].

are determined as 0% - 20% for the most cental collisions, 20% - 40%, and 40% - 100% as is shown in Fig.34.

1.2.2 The nuclear modification factor

The binary collision is an interaction between two free particles; in terms of heavy ion collisions, it is an interaction between two nucleons. The nuclear modification factor R_{AA} or R_{dA} is a ratio of the particle production in nucleus-nucleus (deuteron-nucleus) collisions to the production in proton-proton collisions, scaled by the average number of binary collisions for given centrality. If there is no modification in medium, the production in $A+A$ ($d+Au$) is a simple superposition of the nucleon-nucleon interactions and $R_{AA} = 1$ ($R_{dA} = 1$). The nuclear modification factor R_{AA} is defined as

$$R_{AA} = \frac{dN/dy_{AA}}{N_{coll} dN/dy_{pp}}, \tag{3}$$

where dN/dy is an invariant yield and N_{coll} is the number of binary collisions. If the R_{AA} value is greater than 1, an enhancement is observed, if it is less than 1, a suppression is observed.

1.2.3 Space-time evolution of matter

The evolution of matter created in high-energy heavy ion collisions can be illustrated by a space-time diagram (Fig.3), with the longitudinal coordinate z and transversal coordinate t. It may be viewed as evolving through the following stages that are expected to exist from the initial collision to the final hadronic phase. It is assumed that the space-time evolution depends only on the proper time $\tau = \sqrt{t^2 - z^2}$:

1. At the proper time $\tau = 0$, a huge amount of energy is deposited in a tiny volume. The expected energy density is high enough to form deconfinned matter of quarks and gluons. The matter in this stage is not in the thermal equilibrium. The dynamics in this phase could be described by a cascade of colliding partons.

2. Deconfined state of partons in thermal equilibrium. This phase is called a QGP stage. The QGP then evolves like fluid, expands and cools down according to the hydrodynamic laws.

3. At $\tau = \tau_c$ the system has reached the critical temperature T_c, and starts to hadronize. If the transition is of the first order, matter passes through the mixed phase consisting of gluons, quarks and hadrons.

4. The hadronization of the system is finishing, and hadrons are interacting with each other till the temperature drops to the freeze-out temperature.

5. At the freeze-out temperature hadrons finish interacting and leave the collision region.

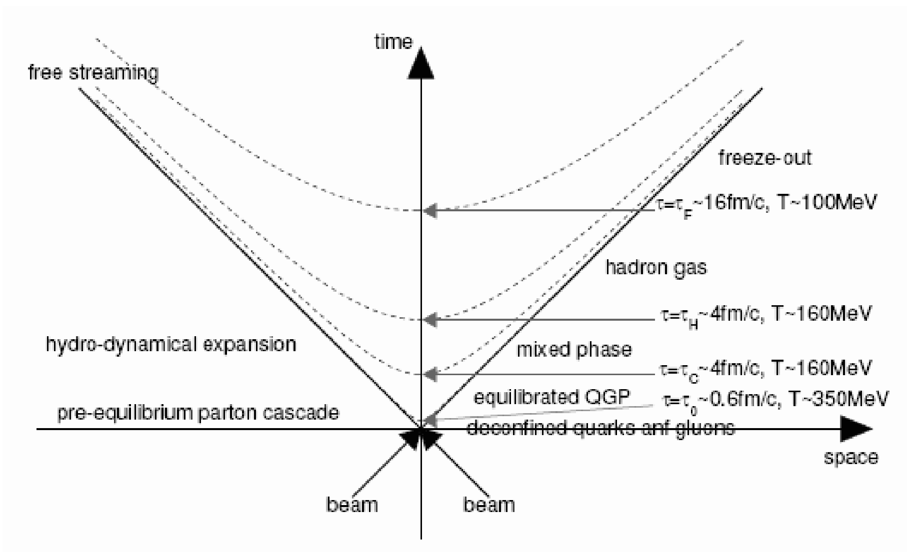

Figure 3: Time space evolution of matter created in high energy heavy ion collisions [7].

1.3 From SPS to LHC

Heavy ion collisions at ultra-relativistic energies are a unique tool to produce and study QGP in the laboratory. First experiments focused on this strong interacting matter were fixed-target experiments, the AGS in Brookhaven ($Au+Au$ $\sqrt{s_{NN}} = 5$ GeV) and at the SPS ($Pb+Pb$ $\sqrt{s_{NN}} = 17$ GeV). Major signs for the production of a QGP at the SPS were, the enhancement of the production of hyperons with respect to the rate from $p+p$ collisions and the J/ψ suppression.

To confirm this results, the Relativistic Heavy Ion Collider (RHIC) began operating. The center-of-mass energy increases with respect to the SPS of a factor 10. Experiments at RHIC, STAR and PHENIX have shown that a very dense QCD medium is formed in high-energy heavy-ion collisions. Other measurements, namely elliptic flow and baryon to meson ratios, indicate that this medium is characterized by partonic degrees of freedom and that its expansion and cooling is well described by hydrodynamical models with high viscosity [12].

Finally, the Large Hadron Collider (LHC) started operation with $p+p$ collisions at $\sqrt{s} = 900$ GeV in the year 2009 and at $\sqrt{s} = 7$ TeV since March 2010. LHC is providing nuclear collisions at a center-of-mass energy up to 30 times higher than at the RHIC. Under such high energy particle production will be dominated by hard processes. That allows the systematic study of the properties of QGP.

2 Charmonia properties and production mechanism

Quarkonium is a bound state of a heavy quark and antiquark pair. Quarkonium composed of a charm quark and antiquark pair is called charmonium, and quarkonium composed of a bottom quark-antiquark pair is called bottomonium. Typical for all quarkonia is their small radium as will be shown later in J/ψ meson.

2.1 Charmonia and its discovery

The schema of charmonium current state knowledge is illustrated in Fig. 4. Charmonium states can be classified by their principal quantum number n. This schema shows charmonia in the ground state (the J/ψ meson and η_c) and in the excited state (the ψ' meson and three states of χ_c). Excited states of charmonia could feed-down to the J/ψ. The feed-down means a decay into the J/ψ meson with photon emission, in the case of χ_c), or with light hadrons production, in the case of ψ'. The feed-down contribution to the J/ψ production will be discussed later in 2.3.

The J/ψ meson was discovered in 1974 simultaneously in two independent laboratories. In Stanford at SPEAR collider in e^+e^- annihilation, by Burton Richter, and in the Brookhaven National Laboratory at the alternating gradient synchrotron (AGS) in $p + Be$ collisions, by Samuel Ting. This new particle decayed slowly and did not fit into the framework of up, down, and strange quarks. The J/ψ discovery was the first firm experimental evidence for the fourth quark. Richter and Ting shared the Nobel Prize for the discovery in 1976.

Properties of the J/ψ meson and the other charmonium bound states are shown in Table 3 [2].

Particle	Mass [MeV/c^2]	Width [MeV/c^2]	Decay mode	Branching ratio
			hadrons	87.7±0.5
J/ψ	3097	0.093	e$^+$ e$^-$	5.94±0.10
			μ^+ μ^-	5.93±0.10
χ_0	3415	10.4	J/ψ + γ	1.30±0.10
χ_1	3511	0.89	J/ψ + γ	35.6±1.9
χ_2	3556	2.06	J/ψ + γ	20.2±1.0
			hadrons	97.9±0.3
ψ'	3686	0.277	J/ψ + X	56.1±0.9
			e$^+$ e$^-$	0.74± 0.18
			μ^+ μ^-	0.73± 0.18

Table 3: Properties of charmonia bound states: mass, width, decay modes and branching ratio.

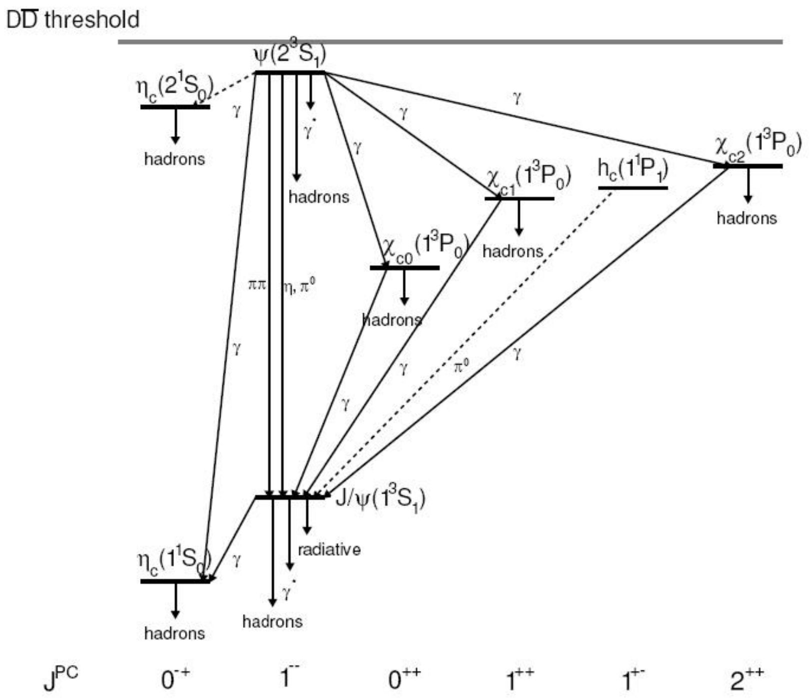

Figure 4: Charmonium model, the current state of knowledge of the charmonium system. The frequent feed-downs are denoted by solid lines, and the dashed line denotes uncertain transitions [7].

2.2 Theoretical model of charmonia production in hadronic collisions

Production of J/ψ from initial partons is divided into several steps. The first step is a $c\bar{c}$ pair production in hard scattering (truly perturbative processes with momentum or mass scales of the order of tens of GeV) of the initial partons, and the finally one is hadronization into J/ψ from the $c\bar{c}$ pair. At high energy, the dominant process of the charm quark and antiquark pair production is a gluon fussion as shown in Fig. 5 [13].

A more elaborate part is obtaining the bound state from a $q\bar{q}$ pair (step 2), especially if the bound state is to be produced with the right angular momentum and spin quantum numbers. Most of the $q\bar{q}$ pairs are not produced as color singlets as required for bound states. These part of charmonia production is not well understood yet; hence there are several theoretical models employed for quarkonium production: the color singlet model (CSM) [14], the color evaporation model (CEM) [16], the color octet model based on nonrelativistic QCD (NRQCD) [15], and the comover enhancement scenario (CES) [17]. However, none of these models succeeded to make the universal description of the

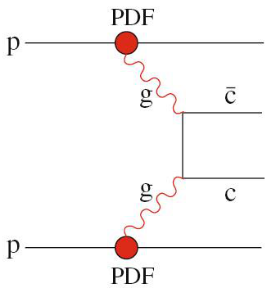

Figure 5: The lowest order Feynman diagram for $c\bar{c}$ production through gluon fusion [13].

quarkonium production. These models are briefly explained in the following subsections.

a) Color singlet model

The color singlet model (CMS) was first proposed shortly after the J/ψ discovery. The CMS requires the colorless $c\bar{c}$ pair to be created with the same quantum numbers as the J/ψ meson. An example of the lowest order diagram of J/ψ production in the CSM, where the $c\bar{c}$ pair has $^3S_1$ and should be colorless as the J/ψ, is shown in Fig. 6.

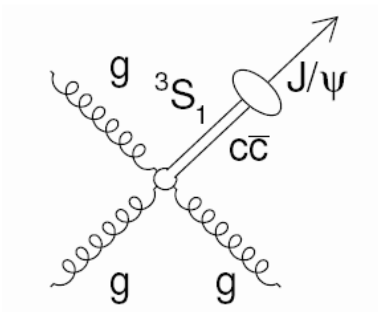

Figure 6: An example of the lowest order diagram for a direct J/ψ production from gluon fusion with the color singlet model. The $c\bar{c}$ pair is in the color singlet state [8].

To conserve C parity, hard gluon emission is necessary in the color singlet model. This model can describe the J/ψ production cross section in the photoproduction, but failed to explain the p_T differential cross section in $p + \bar{p}$ collisions at the Tevatron at the FNAL as is shown in Fig. 7 [20] [21]. Furthermore, in the production and decay of P-wave and higher orbital-angular momentum quarkonium states, the CSM is known to be inconsistent, because it leads to uncanceled infrared divergences [23]. Hence the CSM is theoretically inconsistent for quarkonium states with given nonzero orbital angular momentum.

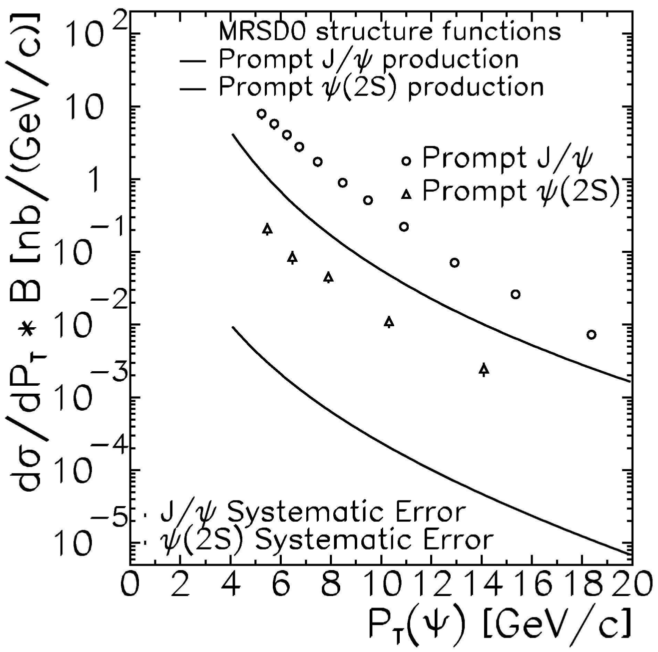

Figure 7: The differential cross section times branching ratio for prompt J/ψ and ψ mesons. Solid lines denote theoretical expectations based on the color singlet model [21].

b) Color evaporation model

The color evaporation model (CEM) was first proposed in 1977. In the CEM model, the quarkonium production is processed in the same way as the open heavy quark production with the restriction that the $c\bar{c}$ mass must be bellow the $D\bar{D}$ threshold [4]. The CEM does not have any constraints on color or other quantum numbers for the $c\bar{c}$ pair. The CEM assumes that the $c\bar{c}$ pair neutralizes its color by an interaction with collision-induced color field, called 'color evaporation'. In the CEM the J/ψ is formed through multiple soft gluon emissions that destroy the information on quantum numbers of the $c\bar{c}$ pair as shown in Fig. 8.

During the evaporation process, the $c\bar{c}$ pair can form charmonium state as well as combine with light quarks to form open charm D mesons. The total subthreshold charm cross section $S_{c\bar{c}}$ can be calculated over the mass range $2m_c < \hat{s} < 2m_D$ as follows [13]

$$S_c\bar{c}(s) \simeq \int_{2m_c}^{2m_D} d\hat{s} \int dx_1 dx_2 g_p(x_1) g_t(x_2) \sigma(\hat{s}) \delta(\hat{s} - x_1 x - 2s), \tag{4}$$

where $g_p(x)$ and $g_t(x)$ are densities, x_1 and x_2 the fractional momenta of the gluons from projectile and target, and σ is the $gg \to c\bar{c}$ cross section.

The basic assumption of the CEM is that particular production cross sections of single charmonia states are a fixed energy independent fraction of the subthreshold charm cross section

$$\sigma_i(s) = f_i S_{c\bar{c}}(s). \tag{5}$$

Constants f_i were determined empirically. As a consequence, the production ratios of different charmonia states must be energy independent. This prediction was compared with obtained data and found well supported [18] [19].

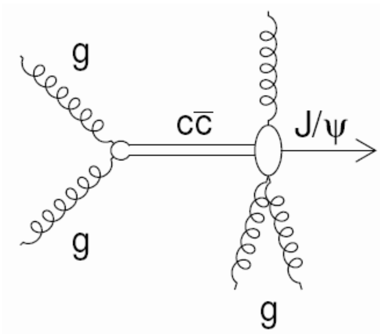

Figure 8: An example of the lowest order diagram for the direct J/ψ production from a gluon fusion with the color evaporation model [8].

In detail, the CEM describes a total hadro-production and photo-production of J/ψ at lower energies. The CEM predicts zero polarization of the J/ψ meson that is consistent in the lower p_T region, but that is not consistent in the intermediate and high p_T regions [8].

c) Color octet model

The color octet model (COM) was developed in the 1990's based on the non-relativistic QCD (NRQCD) framework [4]. The COM allows a J/ψ formation from a color octet $c\bar{c}$ pair with one or few soft gluons emissions. An example of the COM is shown in Fig. 9.

The COM has successfully reproduced the p_T distribution in $p + \bar{p}$ collisions and the total cross section at lower-energy experiments [8]. On the other hand, the COM predicts large transverse polarization, while large longitudinal polarization is observed experimentally as is shown in Fig. 10.

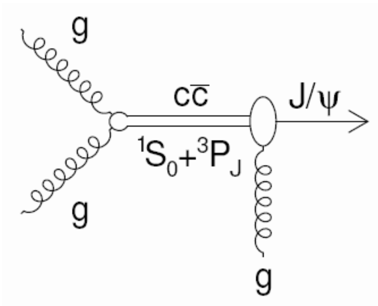

Figure 9: An example of the lowest order diagram for the direct J/ψ production from the gluon fusion with the COM [8].

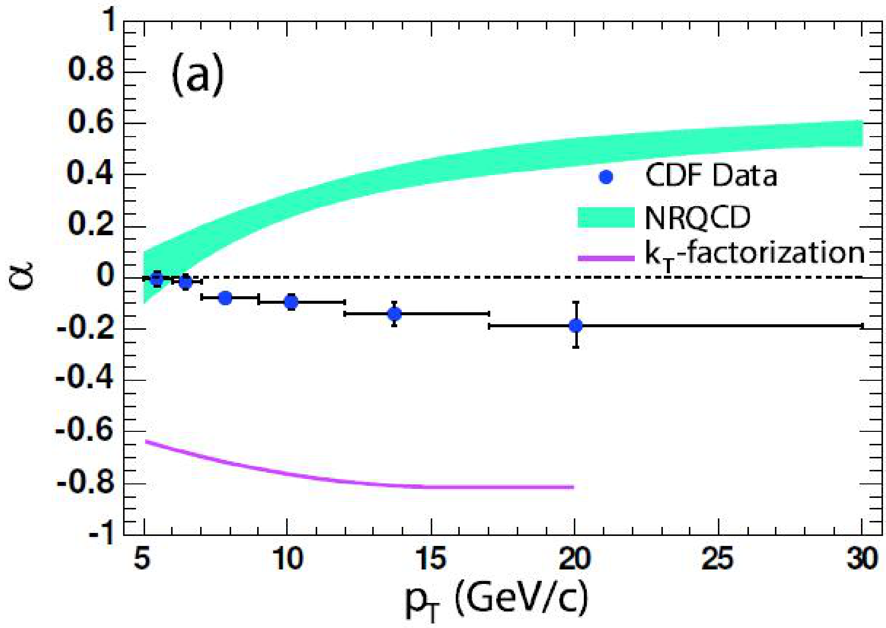

Figure 10: Prompt J/ψ polarization as a functions of p_T. The band and the line are predictions from NRQCD and the k_T - factorization model [22].

2.3 Different channels of J/ψ production

J/ψ mesons actually measured in hadron-hadron collisions could have four different origins: direct production of J/ψ from hard scattering, feed down from three χ_c states, feed down-from a ψ' state, and production from the decay of bottom mesons. The part of (measured) J/ψs from three χ_c states decays is represented by the ratio $R_{\chi c}$, and J/ψs produced from the ψ' state are represented by the ratio R'_{ψ} defined as follows

$$R_{\chi c} = \frac{1}{\sigma_{J/\psi}} \sum_{i=0}^{2} BR(\chi_{ci} \to J/\psi + \gamma)\sigma_{\chi_{ci}}, \tag{6}$$

$$R_{\psi'} = \frac{\sigma_{\psi'}}{\sigma_{J/\psi}} BR(\psi' \to J/\psi + X), \tag{7}$$

where $\sigma_{J/\psi}$ is a J/ψ cross section, $BR(\chi_c \to J/\psi + \gamma)$ is a branching ratio of the $\chi_c \to J/\psi$ decay, and $BR(\psi' \to J/\psi + X)$ is a branching ratio of the $\psi' \to J/\psi$ decay. It was assumed for a long time that the feed-down fraction of J/ψ production is 10% from the ψ' and 30-40% from χ_c states.

These predictions were not based on experimental results till HERA-B collaboration reported a J/ψ feed-down from χ_c decays of considerably lower values than expected (20%) [24]. This number is not the final result yet, and other data sets must be analyze for a more accurate solution. The average value of R_{χ_c} and $R_{\psi'}$, that is on the theoretical base, is about 0.3 and 0.1 [7]. Finally, the fraction of the J/ψ production from a bottom quark decay is represented by the ratio R_b, and is about 0.014 [7]. The fraction of B-meson feed-down was also studied at STAR via azimuthal correlations between higt-p_T J/ψs ($p_T > 5$ GeV/c) and charged hadrons with $p_T > 0.5$ GeV/c. This analysis gives the contribution of B-mesons decays to the inclusive higt-p_T J/ψ production of 13±5% [25]. To sum it up, the contributions to the J/ψ production from the 4 origins are listed in Table 4.

J/ψ origin	$\mathrm{R_{theory}}$	$\mathrm{R_{HERA}}$	$\mathrm{R_{STAR}}$
direct	0.6	$--$	$--$
χ_c	0.3	0.25 ± 0.05	$--$
ψ'	0.1	0.081 ± 0.003	$--$
B - quark	0.01	$--$	0.13 ± 0.05

Table 4: The ratio of the direct and feed-down contributions to the J/ψ production. The second column displays theoretical calculations [7], and the third column experimental results obtained at HERA-B [24].

As will be mentioned in Chapter 3, due to their larger radius than J/ψ, the ψ' and χ_c states are unbound in QGP earlier than J/ψ. This leads to the fact that a significant level of the J/ψ suppression can be observed even if the produced matter has not reached as high temperature and energy density as required in order to melt the directly produced J/ψs. As a consequence, the suppression of J/ψ cannot be immediately, without an extensive study of other charmonia properties, interpreted as a proof of the QGP formation due to the fact that a large fraction of produced J/ψ mesons come from decays of ψ' and χ_n that are affected by the medium in different way than the directly produced J/ψ.

2.4 J/ψ production in hadron-hadron, hadron-nucleus and nucleus-nucleus collisions

Since charm quarks are heavy, the production of charm quarks takes place only in the beginning of the collision. In nucleus-nucleus collisions J/ψ can be formed before QGP formation. The medium effect on the J/ψ production can be categorized into two groups: cold nuclear matter effects, and hot media effects.

The J/ψ production in a nuclear medium is modified as compared to hadronic collisions. This modification of production, suppression or enhancement, is independent of the other effects occured in deconfined medium only. These effects are known as cold nuclear matter effects. The possible contribution to the modification of the J/ψ production are gluon shadowing and nuclear absorption. These effects are observable in $p + A$ and $d + A$ collisions where no new state of the matter is produced, and also play a partial role in $A + A$ collisions. Therefore the study of these collisions provides a great tool to analyze charmonium production, evolution and absorption in a confined matter. The cold nuclear matter effect is described in Chapter 4.

On the other hand, in $A + A$ collisions under sufficiently high temperature, the hot media effects take place. There are following contributions to the modification of the J/ψ production: color screening in QGP, recombination of J/ψs from uncorrelated $c\bar{c}$ pairs, and the J/ψ interaction with secondary comovering hadrons. The hot media effects are described in Chapter 3.

3 Charmonia in hot and dense matter

As a result of color screening, J/ψ meson could be unbound in a hot and dense medium, and charm quark and antiquark are separated. After freeze out the distance between them is too large to recompound into a bound state again. Since the thermal production of an additional charm quark-antiquark pair is negligibly small, these unbound c and $\bar{c}$ quarks interact with a light antiquark or quark to form open charm mesons. Therefore the presence of a hot and dense medium leads to a suppression of J/ψ. In this Chapter the Schwinger potential model of the suppression and the other hot media effects is described.

3.1 Color screening

The screening is a global feature of a medium that is shortening the range of the binding potential.

3.1.1 The charmonia potential and the screening mass

Because of the large charm quark mass, the charmonium spectrum can be calculated with good a precision by means of the non-relativistic Schrödinger equation [26]

$$[2m_c - \frac{1}{m_c}\nabla^2 + V(r)]\psi_{n,l} = E_{n,l}\psi_{n,l}. \tag{8}$$

For different values of the principal quantum number n and the orbital quantum number l, the eigenvalues $E_{n,l}$ and the wave functions $\Psi_{n,l(r)}$ belong to different charmonium states $J/\psi, \Psi', \chi_n, \eta_c$. The potential V defined as

$$V(T=0,r) = \sigma r - \frac{\alpha}{r}, \tag{9}$$

and known as Cornell potential is spherically symmetric and contains a confining long-distance part σr corresponding to the confining potential obtained in the calculation of the Wilson loop, and a Coulomb-like short-distance part $\frac{\alpha}{r}$ originating from the gluon exchange between quark and antiquark, where r is a $q\bar{q}$ separation, σ is a string tension that is determined by the strength of a confining term, and α is the coupling constant.

This simplyfied potential can be used to describe the quarkonia bound state in $p+p$ and $d+Au$ collisions. The potential does not account for spin-orbit or spin-spin couplings that are needed to separate the three χ_c states or to separate the J/ψ from the η_c respectively, but it is sufficient for our purposes. In a medium, the potential is modified, i.e.

$$V(T,r) = \frac{\sigma}{\mu}(1-\exp^{-\mu r}) - \frac{\alpha}{r}\exp^{-\mu r}, \tag{10}$$

where μ is the screening mass, and its reciprocal value is the Debye screening length, λ_D. Due to its linear propotion to the temperature, it is more convenient use this parameter in the form of a screening mass. Using finite temperature lattice QCD, we can determine the screening mass μ as a function of the temperature T or, equivalently, as a function of the energy density ϵ of the medium. The screening mass μ is defined as

$$\mu(T) = \sqrt{\frac{N_c}{3}\frac{N_f}{6}g^2T}, \tag{11}$$

where N_c is the degree of color freedom, N_f is the number of quark flavors, $g^2 = 4\pi\alpha$, and T is the matter temperature.

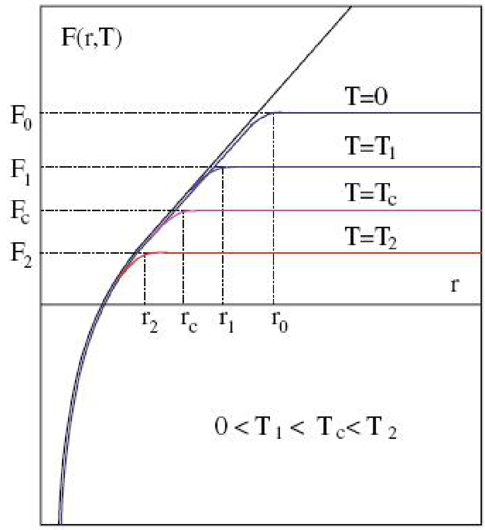

Figure 11: Deconfinement by color screening, the string-breaking radius dependence on temperature [26].

Once μ becomes sufficiently large, the bound states begin to disappear, starting with the weakest bound. Each binding state has its radius and when the Debye screening length for a given system under the defined conditions is smaller than the distance between quark and antiquark, the bound state exists no longer. A simple schema of the string braking radius as a function of a temperature is shown in Fig. 11.

The temperature requested for deconfine charm quarks was calculated using various potential models with different parameterizations of the heavy quark potential [27] [28] [29] [30]. All these models predict that the temperature necessary for dissolution of the ground charmonium bound state J/ψ is in the range from 1.1 T_c to 1.3 T_c.

Recently, charmonium properties have been investigated using lattice calculations as well [31] [32], indicating that the ground states exist with essentially unchanged properties at temperatures around 1.5 T_c.

Since J/ψ has a smaller radius than the other quarkonia states, the required energy density is double than for Ψ', χ_n, and the dissociation temperature is significantly higher. As mentioned before, the J/ψ's are not all directly produced, but they have four different origins. A fraction of the J/ψ production originates from ψ', B-quark, χ_n decays. As a consequence, the nature of the J/ψ suppression has more then only one origin, and J/ψ can be suppressed at a lower temperature because the feed down contribution to the production vanish before the temperature is high enough for the J/ψ dissociation. At first, J/ψ's originated from ψ' dissapear, then that from χ_c, and only a considerably higher temperature is able to remove the directly produced J/ψ's. Hence, the measurement of J/ψ suppression can be used as a QGP thermometer, as shown in Fig. 12. All suppressions in hot and dense medium observed on SPS and RHIC originate in the above described sequential suppression, since the produced matter does not reach energy densities high enough to melt directly produced J/ψs [13]. To observe a direct J/ψ suppression is possible only on LHC.

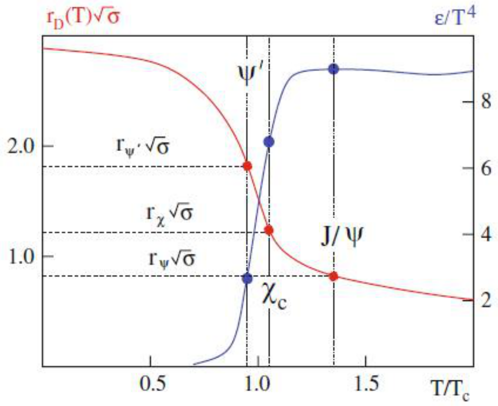

Figure 12: The charmonia suppression as a thermometer [8].

3.1.2 Time evolution of J/ψ formation

One of the essential question that is necessary to be answered is if J/ψ mesons can escape from the production region before plasma formation. Time scales of the $q\bar{q}$ pair production and charmonia formation can help to answer it. The time τ_0 required to form plasma in thermal equilibrium is expected to be 0.6 fm [33]. The $c\bar{c}$ pair production time can be obtained from the uncertainty principle

$$\tau_{c\bar{c}} m_c \sim \frac{\hbar}{2}, \tag{12}$$

where m_c is the expected charm quark mass. For $m_c = 1.6$ GeV, the pair production time is $\tau_{c\bar{c}} = 0.06$ fm. Another time that must be taken into account is the formation time, τ_f. It is time necessary for a formation of J/ψ from a $c\bar{c}$ pair. The formation time is different for each quarkonia bound state. It depends on the radius and on the relative velocity of the $q\bar{q}$ pair. This formation time is of the order τ_0 except for the situation $r_{J/\psi} << r_h$, where $r_{J/\psi}$ and r_h are radii of the J/Ψ meson and the typical hadron respectively. And this is not the case as will be mentioned later. Hence, J/ψ cannot be formed before plasma formation. And last but not least, J/ψ formed in nucleon-nucleon collision still have to travel a distance of $r \sim A^{1/3}$, where A denotes the nuclear mass number.

3.1.3 J/ψ radius

For a $c\bar{c}$ pair in vacuum, the typical values are $\sigma \approx 0.16$ GeV^2, $\alpha \approx 0.52$ [1]. The energy of the bound state can be estimated semi-quantitatively as

$$E(r) = 2m_c + \frac{1}{2m_c r^2} - \frac{\alpha}{r} + \sigma r, \tag{13}$$

including the charm quark rest masses m_c and their kinetic energy. To find the lowest state (as mentioned before, J/ψ is the ground state of charmonia), we minimize E(r)

$$0 = \frac{1}{m_c r^3} - \frac{\alpha}{r^2} - \sigma. \tag{14}$$

With beforehand noticed values of σ and α and $m = 1.56$ GeV, the minimum energy is 3.1 GeV. These values give a radius of the J/ψ meson to be $r_{J/\psi} =$ 0.2 fm. If recalculated with other parameter values (smaller $m_c = 1.3$ GeV - in the case that the binding energy of J/ψ is bigger; smaller α) a larger radius of the bound state is obtained. Therefore, we can consider that J/ψ radius is laying in the range $0.2 < r_{J/\psi} < 0.5$ fm. Although $r_{J/\psi}$ is smaller than the radius of conventional mesons it is still in agreement with the hadronic scale.

3.2 The other hot media effect

The last question that must be asked and resolved is, if there are any other non-plasma suppression or enhancement mechanisms. These mechanisms known as cold nuclear matter, included nuclear shadowing, and nuclear absorption will be discussed in detail in Chapter 4. A pragmatic definition of cold and hot effects is as follows: what can occur in $p + Au$ or $d + Au$ collisions is CNM effect, and additional effects that can occur only in $Au + Au$ collisions are hot nuclear matter effects. Other hot nuclear effects, the J/ψ recombination and interactions with comovers will be mentioned briefly now.

3.2.1 J/ψ recombination

Not only charmonia suppression can be observed in high energy collisions. Also J/ψ production can be enhanced due to the uncorrelated $c\bar{c}$ pairs recombination. This scenario is predicted at RHIC energies, and it is derived from the assumption that the number of recombined charmonia are approximately proportional to N_c^2/N_h, where N_c is the number of created charm quarks, and N_h is the number of produced hadrons. The charm production N_c increases faster with $\sqrt{s}$, and scales with the number of inelastic nucleon-nucleon collisions, while N_h scales with the number of participant nucleons. Since the number of nucleon-nucleon collisions is sufficiently higher than the number of participant nucleons at RHIC energy in more central collisions, N_c^2/N_h leads to a higher value at a higher collision energy and in more central collisions.

Hence, this effect cannot be negligible at the RHIC energy. Kinematics observable of these secondary charmonia have a different distribution than the primary ones, their rapidity distribution is narrower, and their p_T distribution is lower. There are different models as kinetic formation [34], transport model [35], statistical coalescence [36], and hadron-string dynamics [37] that calculate the recombination of J/ψ from $c\bar{c}$ pairs or $D\bar{D}$ pairs.

3.2.2 Comover interactions

An additional absorption of J/ψ by secondary hadrons called comovers occurs in the hadronic phase. These secondaries, formed after $\tau_0 \approx 1 - 2$ fm, may also scatter with the $q\bar{q}$ pair or with the quarkonium state. As mentioned above, the typical time of quarkonium formation is less than τ_0, and therefore it is assumed that quarkonia are interacting with comovers. The survival probability of J/ψ can be expressed as follows

$$S_{co} = \exp\left(-\int d\tau \rho_{co}(\tau)\sigma_{co} v\right), \tag{15}$$

where τ is time, ρ_{co} is the comovers density, v is the relative velocity between the J/ψ and a secondary hadron, and σ_{co} is a cross section of the J/ψ absorption by comovers [4]. The interactions with comovers lead not only to the charmonia dissociation, but also to their recreation via the inverse recombination process

$$D + \bar{D} \to c\bar{c} + m, \tag{16}$$

where m represent a light quark meson as π, ρ, ω. The inverse comover dissociation cross section are not known very well, and the significance of these channels are under the discussion in presence [38].

3.3 J/ψ suppression at RHIC

Results from the J/ψ measurement at the RHIC in $d + Au$ collisions at $\sqrt{s} =$ 200 GeV have two puzzling features, the fact that the suppression at mid-rapidity is equal to the level of suppression in observed in $Pb + Pb$ collisions at $\sqrt{s} = 17.3$ GeV for the same number of participants, and the stronger suppression at the forward rapidity than at the mid-rapidity [39]. Results for J/ψ suppression at RHIC are shown in Fig. 13.

Since the medium produced at the RHIC has higher density and temperature, and the temperature of medium in a central part is sufficiently higher, it was expected the strongest suppression at mid-rapidity region at RHIC. Supposed reasons of these unexpected results are the fact that nuclear absorption

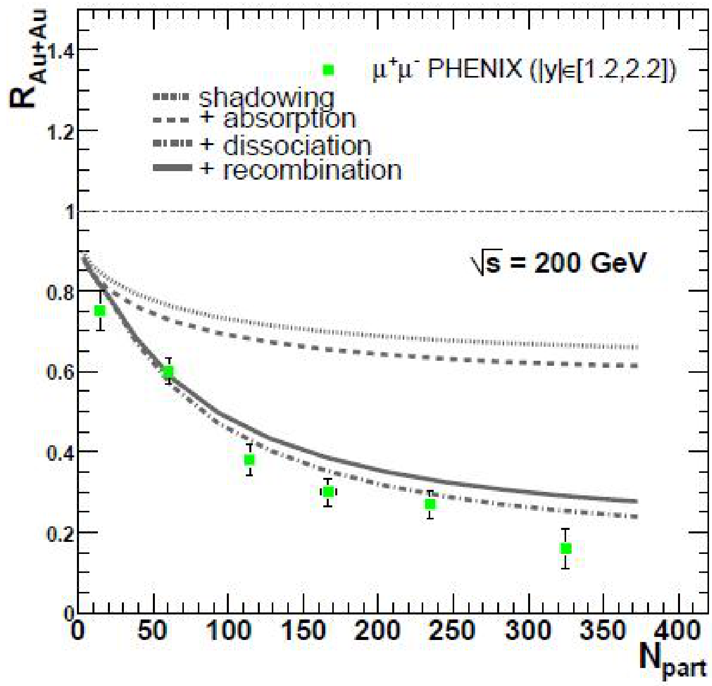

Figure 13: Results for J/ψ suppression in $Au + Au$ collisions at RHIC at $\sqrt{s} = 200GeV$ at forward rapidity region. Solid lines denote the final results. Dash-dotted curves are results without recombination. The dashed line shows the total initial-state effect. The dotted line is the result of shadowing [39].

is presented at forward rapidity only, and J/ψ recombination is larger at mid-rapidity region. Consequently, the role of initial state effects and J/ψ recombination are studied in more detail. It is assumed much larger magnitude of both effects at LHC energies.

4 Cold nuclear matter effects

The name cold nuclear effects (CNM effects) come from the fact that these effects are observed in hadron-nucleus interactions where no hot and dense matter is present, as in nucleus-nucleus collisions. Considered CNM effects are a modification of a parton distribution function (i.e. nuclear shadowing), the parton energy loss before hard scattering, and the nuclear absorption of a quarkonium. The first and the second effects are calculated into initial-state effects, and the absorption is the only cold nuclear matter effect counted among final-state effects. The nuclear matter dependance on nuclear hard processes is usually parameterized as a power law, based on empirical observations [40]

$$\sigma_{AB} = \sigma_N N(AB)^{\alpha}, \tag{17}$$

$$\sigma_{NA} = \sigma_N N(A)^{\alpha}, \tag{18}$$

for nucleus-nucleus Eq. 17 and hadron-nucleus Eq. 18 collisions, respectively, where an exponent α represents all nuclear effects and depends on x_F, p_T and $\sqrt{s_{NN}}$. Nuclear shadowing and nuclear absorption are described in Chapter 4.1 and Chapter 4.2 subsequently.

4.1 Nuclear shadowing

Parton density in a free proton is different from that in a nucleus. Therefore, the nuclear structure function, that characterized the inner structure of nucleus is different from the superposition of its constituents particle structure functions (PSF characterized inner structure of particle, in case of proton-proton collisions the internal structure of the proton). This phenomena have been proved in deep inelastic scattering (DIS) of leptons on a nucleus and nucleon [41] that have been used to constrain free PSF. This parton distribution modification depends on the parton momentum fraction x_F and at square of the momentum Q^2 and it is quantified by nuclear ratio that is defined as

$$R_i^A(x, Q^2) = \frac{f_i^A(x, Q^2)}{A f_i^N(x, Q^2)}, \tag{19}$$

where A is the nuclei mass number and f_i is a parton distribution function for quark, antiquark and gluon. The R_i^A ratio as a function of the Bjorken x_F has been measured in a large range of x_F values, and the results are listed in Tab. 5 and schematically figured in Fig. 15.

The most important nuclear ratio considered in the study of J/ψ production is that for gluons, since the gluon fusion is the dominant production process of the charm quark and antiquark. Therefore, gluon shadowing has a significant impact on J/ψ production. The gluon modification ratio R_g^A as a function of x_F is shown in Fig. 15. Lines denote different models, and shaded boxes indicate the x_F probed in different experiments, from the top to the bottom: NMC, SPS, FNAL, HERA-B, and RHIC. While anti-shadowing is expected at SPS energies, a suppression of the J/ψ production is expected at RHIC energies.

x_F	R_F^A	effect
$x_F < 0.1$	< 1	shadowing
$0.1 < x_F < 0.3$	> 1	antishadowing
$0.3 < x_F < 0.8$	< 1	EMC
$0.8 < x_F$	> 1	Fermi smearing

Table 5: List of nuclear effects and their R_F^A ratios as a function of x_F [42].

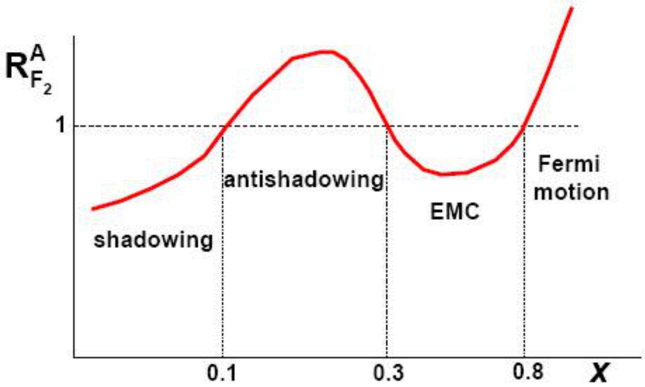

Figure 14: Nuclear effects as a function of x_F [41].

4.2 Nuclear absorption

The second CNM effect that must be taken into account is nuclear absorption. The nuclear absorption refers to the probability for a pre-resonant $c\bar{c}$ pair to survive the propagation through the nuclear medium, and is usually parametrised by introducing an effective absorption cross section $\sigma_{abs}^{c\bar{c}}$. The probability that a charmonium traverses the target nucleus without any interactions with the nuclear matter can be calculated as

$$S_{abs}^{c\bar{c}} = \frac{1}{A}\int d^2b \int dz \rho_A(b,z) S_{abs}^{c\bar{c}}(b,z), \tag{20}$$

where b is the impact parameter, z is the $c\bar{c}$ production coordinate along the beam axis, ρ_A is the nuclear density profile (mostly used the Woods-Saxon model), and $\sigma_{abs}^{c\bar{c}}$ is the $c\bar{c}$ break up cross section.

Finally, the nuclear modification factor R_{dAu} measured at PHENIX in $Cu+Cu$ collisions at $\sqrt{s_{NN}} = 200$ GeV is shown in Fig. 16 compared to the EKS [44] model that was mentioned above [50]. The reported J/ψ suppression and enhancement as a function of the rapidity is a product of full cold nuclear matter effects set.

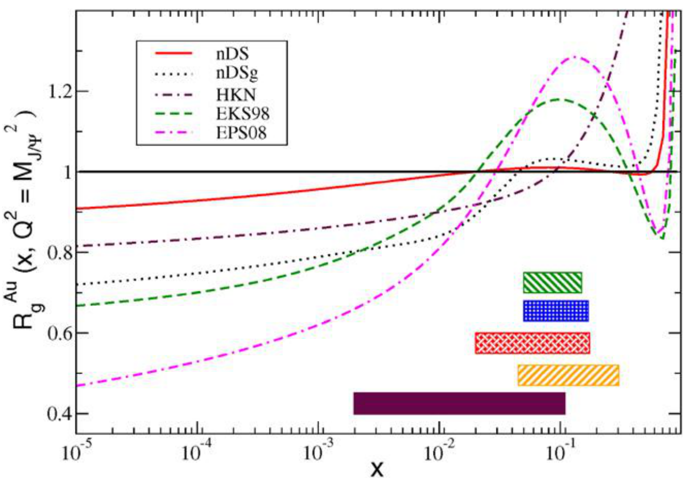

Figure 15: The ratio of the gluon distribution in a gold nucleus, $R_g^{Au}(x_F, Q^2)$ as a function of the Bjorken x_F using the nDS, nDSg [43], EKS98 [44] [45], HKN [46] [47] and EPS08 [48] parametrizations. The bands indicate the typical x_F ranges from J/ψ production in the NMC, SPS, FNAL, HERA-B, and RHIC experiments, from the top to the bottom [49].

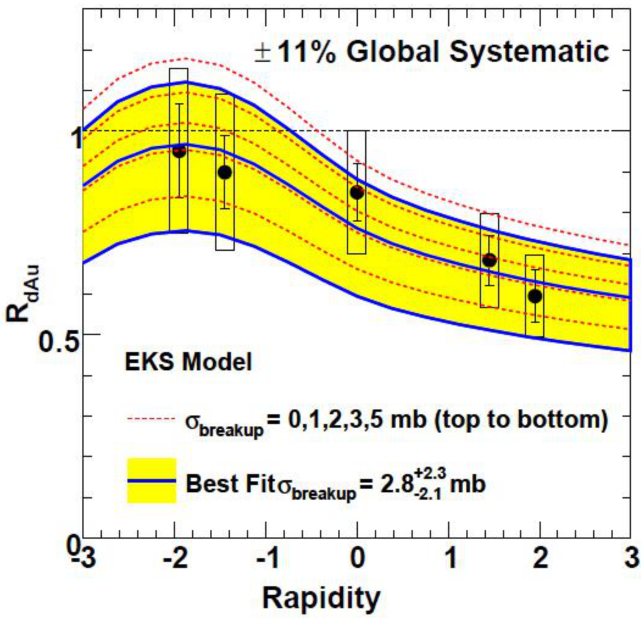

Figure 16: Nuclear modification factor R_{dAu} measured at PHENIX in $Cu + Cu$ collisions at $\sqrt{s_{NN}} = 200$ GeV compared to the EKS [44] model [50].

5 J/ψ measurement at STAR

In this Chapter the results from the STAR experiment are presented. The recent results were recently summarized in these proceedings [51] .Namely, the high-p_T J/ψ production in $p+p$ and $Cu+Cu$ collisions at $\sqrt{s_{NN}} = 200$ GeV from data taken in the years 2005 and 2006, and the low-p_T J/ψ production in d+Au collisions at $\sqrt{s_{NN}} = 200$ GeV from the year 2008. The low-p_T J/ψ trigger based on information from the central trigger barrel was used for electron selection from the photon background in $p+p$ (2006) data. Since 2009 the low-p_T J/ψ trigger is based on information obtained by TOF detector and it is provide better background rejection together with sufficient signal efficiency.

5.1 J/ψ production in $p+p$ and $Cu+Cu$ collisions

At first the J/ψ production at high transverse momentum in $p+p$ and $Cu+Cu$ collisions at $\sqrt{s_{NN}} = 200$ GeV is discussed. The $Cu+Cu$ data are from year 2005 measurements, and the $p+p$ data are from the years 2005 and 2006. The $Cu+Cu$ data were analyzed in two centrality classes, $0-20\%$ and $0-60\%$ most central collisions. The J/ψ signal was reconstructed via the dielectron decay channel with branching ratio 5.9%. Using information from the TPC (dE/dx) and the BEMC (shower energy), electrons and positrons were identified with the purity of the achieved sample $> 70\%$ and high reconstruction efficiency [25]. The J/ψ invariant mass spectrum is shown on the left side in Fig. 17 [25], in $p+p$ collisions on the top, and in $Cu+Cu$ collisions on the bottom.

The J/ψ yield was extracted by subtracting the like-sign pairs invariant mass spectrum from the unlike-sign pairs. The like-sign background is marked on the left part of Fig. 17 as the gray band. The peak was fitted, and the number of found J/ψ was calculated in the invariant mass region $2.7 < M_{J/\psi} < 3.2$. After that the J/ψ reconstruction efficiency was estimated by embedding simulated J/ψ's into real events [25]. The p_T of J/ψ spectra in $p+p$ and $Cu+Cu$ collisions such as perturbative theoretical calculations except the feed down contribution to the J/ψ production is shown on the right side of Fig. 17 [25]. The CS+CO calculation (solid line) describes the data well, with a little empty area for a feed-down contribution.

The nuclear modification factor R_{AA} is the ratio of the yield in nuclear collisions to that in p+p collisions scaled to one nucleon-nucleon collision. This factor is used to quantify medium-induced effects on particle production. The R_{AA} factor for J/ψ at high-p_T in $p+p$ and $Cu+Cu$ collisions compared to that measured at PHENIX is shown in Fig. 18. The dashed line, the solid line, the dash-dotted and the dotted one represent different theoretical predictions. It is seen that R_{AA} increases with increasing p_T. The average R_{AA} measured at STAR in $Cu+Cu$ collisions is 1.4±0.4(stat.)±0.2(syst.) [25]. Both results for high-p_T J/ψ, that from STAR such as that from PHENIX data are consistent with each other, and differ by two standard deviation from low-p_T result from PHENIX, where $R_{AA} = 0.52$ [52]. This suggests that there is no significant suppression observed at high p_T.

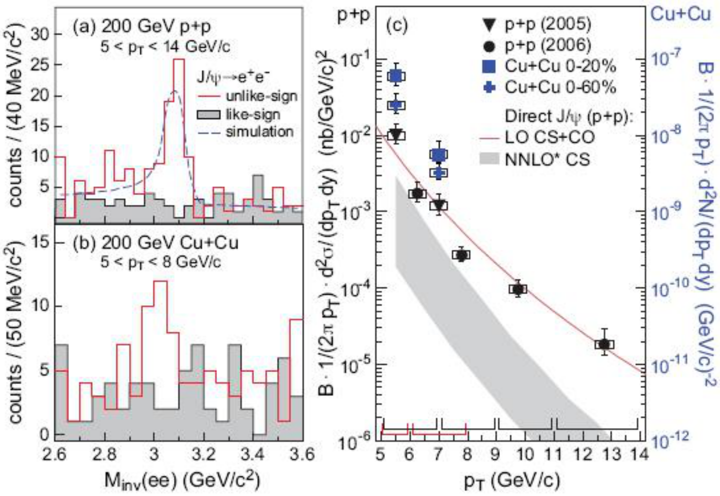

Figure 17: The dielectron mass spectrum in $p+p$ (up) and $Cu+Cu$ (down) collisions. The solid line denotes the unlike sign signal, and the gray zone is the like-sign background on the left, and the J/ψ p_T distributions in $p+p$ and $Cu+Cu$ collisions at $\sqrt{s_{NN}} = 200$ GeV on the right. The solid line and the grey band present the perturbative calculations for CS and CO models (the red line) and for NNLO* CS. Both these calculations have been done without feed-down contribution [25].

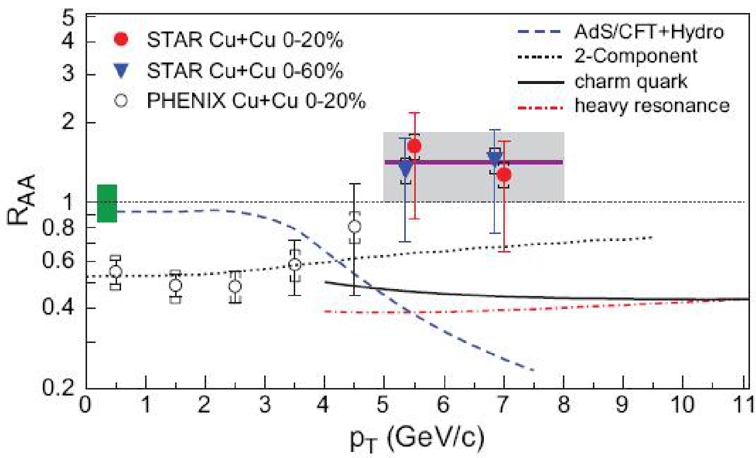

Figure 18: The J/ψ modification factor R_{AA} factor in $Cu+Cu$ collisions at $\sqrt{s_{NN}} = 200$ GeV as a function of J/ψ p_T [25].

The result mentioned above can be related to the fact that initial state effects such as anti-shadowing play an appreciable role and may lead to the increasing J/ψ production with increasing p_T [25].

The azimuthal correlation between high-p_T J/ψs and charged hadrons with $p_T > 0.5$ GeV/c in $p+p$ collisions at 200 GeV is shown in Fig. 19. To attach a better signal to the background ratio, the used invariant mass region was narrower in comparison with the R_{AA} factor calculation, 2.9< $M_{J/\psi}$ <3.2 GeV/c^2. No significant correlation between charged hadrons and higt-p_T J/ψ meson in the near side ($\Delta\theta \approx 0$). The lines denote simulations from PYTHIA: prompt J/ψ, feed down from B-meson, and their sum. This gives the contribution of B-mesons decays to the inclusive J/ψ production of $13 \pm 5\%$ [25].

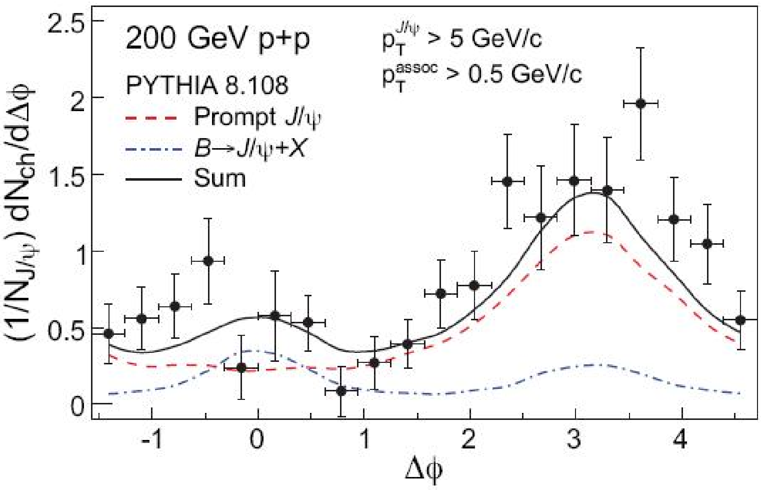

Figure 19: J/ψ - hadron azimuthal correlations. The dashed line and the dash-dotted line denote prompt and B-meson feed-down contributions (PYTHIA), and the solid line shows their sum [25].

5.2 Low-p_T J/ψ production in $d+Au$ collisions at $\sqrt{s_{NN}} =$ 200 GeV

In this subchapter the results from parallel and independent analysis of the J/ψ production in $d+Au$ collisions at $\sqrt{s_{NN}} = 200$ GeV are presented. The data used for this analysis were obtained with the STAR detector during the run 8 (year 2008). The J/ψ yield was reconstructed via the dielectron decay channel. Trajectories of the charged particles were reconstructed in the TPC, and at least one hit in the BEMC tower was required. Then electrons and positrons were identified using dE/dx information from the TPC. The dilepton invariant mass spectrum before background subtraction is shown in Fig. 20, where the black dots indicate the signal obtained from opposite-sign particles, and the red line denotes the like-sign pair background. The J/ψ signal after background subtraction is depicted in Fig. 21, where the red line denotes the J/ψ peak and the residual background.

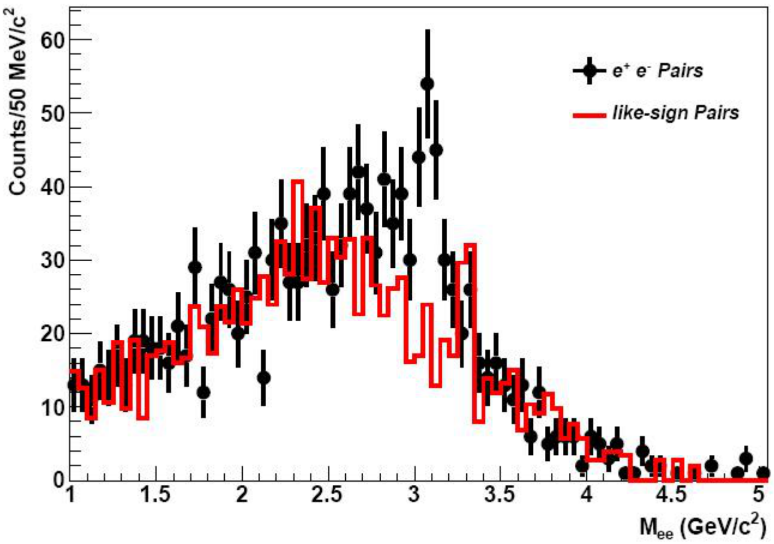

Figure 20: The dilepton invariant mass spectrum. Red line denotes like-sign background [54].

To obtain the true number of produced J/ψ, the efficiency of the analysis and the electron sample purity were calculated. The reconstruction efficiency was determined by embedding, when simulated J/ψ's were embedded into real events and were passed through the same analysis cuts as the real data. The efficiency is defined as a fraction of J/ψ's that satisfy these cuts to all simulated. The invariant yield as a function of the transversal momentum is shown in Fig. 22, where the obtained data are fitted to a power-law function in the form $f(p_T) \sim A(1 + \frac{p_T}{B}^2)^{-6}$.

Finally, the nuclear modification factor R_{AA} was calculated for three centrality classes, 0-20% most central collisions, 20-40%, and 40-100%. The R_{AA} factor is shown in Fig. 23, and is compared with PHENIX data and with a theoretical prediction. The results presented in this paper are from independent analysis of the same data to reconstruct J/ψ as presented in this thesis.

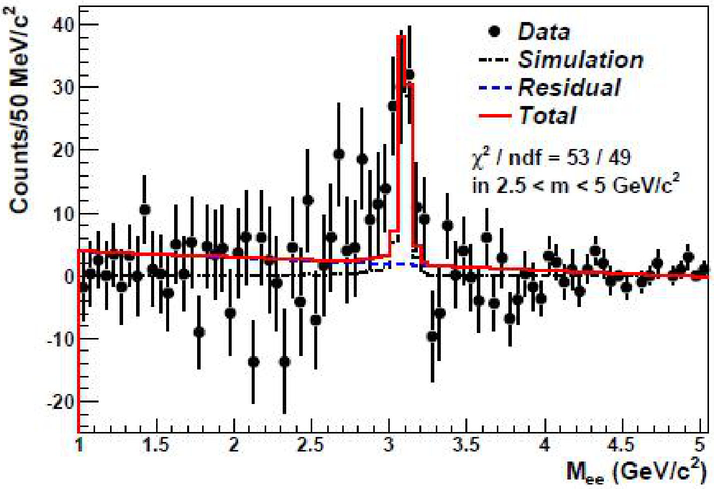

Figure 21: The J/ψ signal after background subtraction. The red line shows the yield and the rezidual background [54].

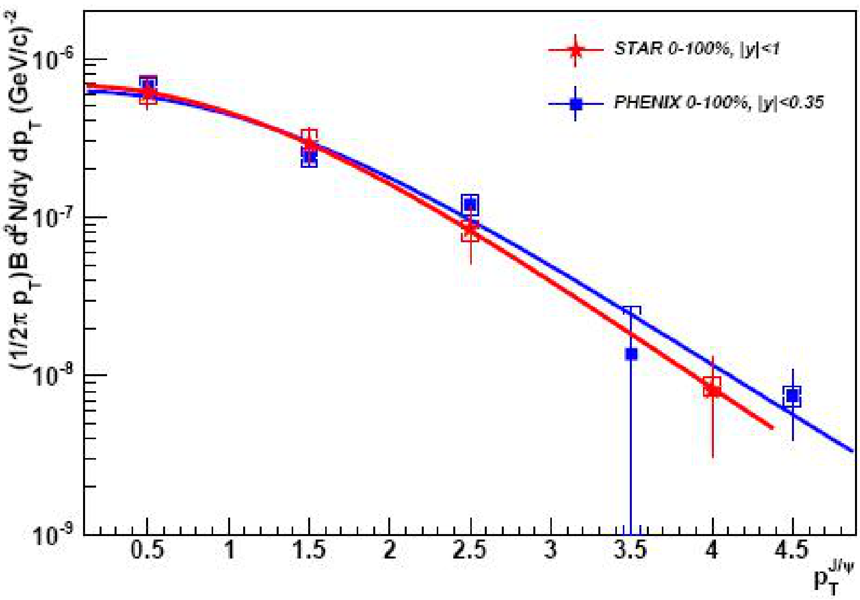

Figure 22: The invariant yield as a function of J/ψ p_T [54].

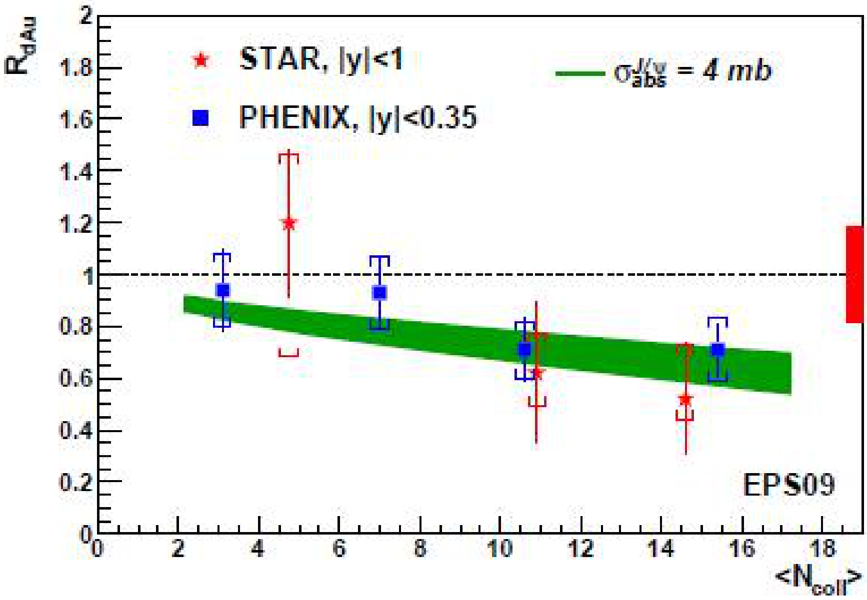

Figure 23: The nuclear modification factor R_{AA} measured at STAR (red) compared with the PHENIX result (blue) and with a theoretical prediction (green band) [54].

6 RHIC and the STAR detector

The Relativistic Heavy Ion Collider (RHIC) is located at the Brookhaven National Laboratory in Upton, New York. The RHIC started its operation in 2000. The whole RHIC complex is illustrated in Fig. 24. Research at the RHIC is focuses on the study of quark gluon plasma, the primordial state of matter that existed in the early universe. Key features of the nuclear environment at the RHIC are a large number of produced particles and a production of high momentum particles from hard parton-parton scattering. The goal is to obtain a fundamental understanding of the microscopic structure of these hadronic interactions at high energy densities [55]. In this Chapter, the RHIC system and the STAR experiment is described in detail.

Figure 24: A schematic view of the RHIC complex [56].

6.1 The Relativistic Heavy Ion Collider

The RHIC is an intersection storage ring (ISR) particle accelerator composed of two independent rings. It is designed to collide light nuclei as polarized protons and heavy nuclei such as Cu, Au and U. Also $d + Au$ collisions can be measured. These asymmetric collisions are important to study cold nuclear matter effects and to distinguish them from hot nuclear matter effects that were described in previous Chapters 3 and 4. The RHIC has a circumference of 3834 m and six intersection points, where particles collide. Originally, there were four experiments at intersection points: STAR, PHENIX, BRAHMS and PHOBOS. BRAHMS and PHOBOS completed their program already. The maximum center of mass energy per nucleon-nucleon pair for $Au + Au$, $d + Au$ and $Cu + Cu$ collisions is $\sqrt{s_{NN}} = 200$ GeV. Protons can be collide up to 500 GeV.

Before reaching the RHIC storage ring, each particle passes through several stages that are illustrated in Fig. 24. Heavy ions started their acceleration in the Tandem Van de Graaf, where ions are accelerated to an energy of about 1 MeV per nucleon. Then ions are stripped of electrons and passed through the Tandem-to-Booster line, the Booster synchrotron. After having passed through the Booster line, ions have an energy of about 95 MeV per nucleon. The next station on the way to the RHIC is the Alternating Gradient Synchrotron (AGS) that was used for fixed target experiments in the past, and where ions are accelerated to an energy of 8.86 GeV per nucleon. Finally, ions are sent through the AGS-To-RHIC (ATR) transfer line. At the end of this process, ion bunches are sent by switching magnets to one of two beam lines. Then the bunches are colliding in one of four interaction point.

6.2 The STAR

The Solenoidal Tracker at the RHIC (STAR) is a massive detector that was designed especially for a study of the hadron production and the search for signatures of the quark gluon plasma formation and its properties and for studies of other physical effects, which occur under extreme conditions in a relativistic heavy-ion collision.

Compared with other experiments at the RHIC, it is unique in its full azimuthal coverage that makes possible a study of azimuthal particle correlations. Due to this and a good coverage of pseudo-rapidity $|\eta| < 1.8$, the STAR detector is able to measure a wide variety of physical phenomena [55].

Most constituents of the STAR experiment are inside a large solenoidal magnet with an approximately uniform magnetic field (B=0.5T maximally) parallel to the beam pipe. The most central tracking detector is the Time Projection Chamber (TPC) that is discussed in detail in Chapter 6.3. The TPC can record only charged particles, although the decay vertices from neutral hadrons can be reconstructed from tracks of charged decay products left in the TPC. The TPC is a strong tool for particle identification, similarly to the Time of Flight detector (TOF, Chapter 6.4) based on the Multi-gap Resistive Plate Chamber (MRPC) technology [58]. Another important part of the STAR detector is the Barrel Electromagnetic Calorimeter (BEMC) that will be discussed in more detail further (Chapter 6.5). The general STAR detector schema is shown in Fig. 25. The Heavy flavor tracker (HFT) and the Forward GEM tracker (FGT) are not implemented right not and they are planned to be ready in 2012 and July 2011 respectively.

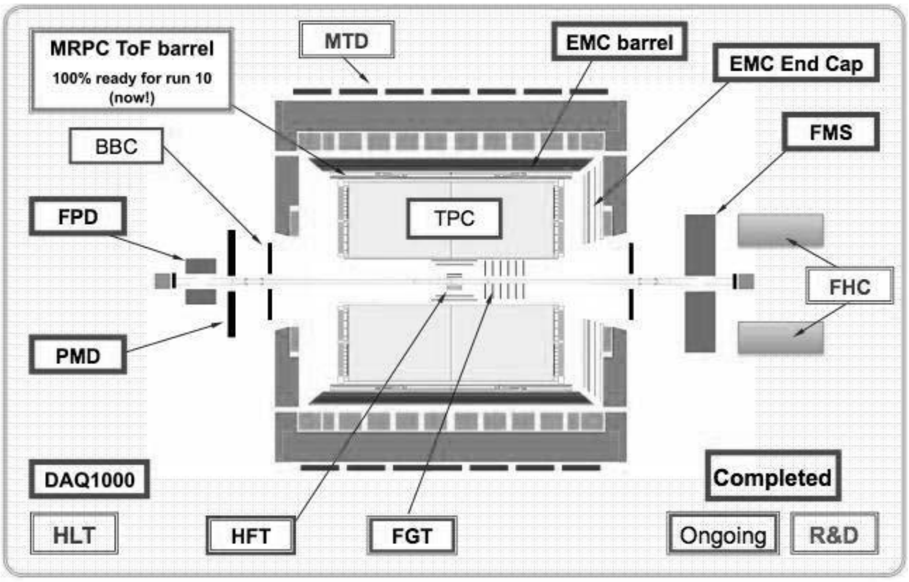

Figure 25: The experimental setup of the STAR detector.

6.3 The Time Projection Chamber (TPC)

The Time Projection Chamber (TPC) is a central element of the STAR detector, located in the solenoidal magnet that surrounds the interaction vertex. The schema of the TPC is shown in Fig. 26. Since the TPC plays key role in an analysis presented in this thesis, we describe it in detail. The TPC has 4.2 m along the beam axis, and 4 m in a diameter, and it is a primary tracking device of the STAR detector that registers tracks of particles, measures their momentum, and identifies particles via the ionization loss energy (dE/dx). Its acceptance covers ± 1.8 units of pseudo-rapidity through the full azimuthal angle. Charged particles with momenta greater than 100 MeV/c are recorded. More than 3000 tracks per event are routinely reconstructed [57].

The TPC is an empty volume filled with an argon-methane gas mixture (10% of methane, 90% of argon) regulated at 2 mbar above the atmospheric pressure. This gas was chosen with respect to its minimum attenuation of drifting secondary electrons. Its primary attribute is fast drift velocity that peaks at a low electric field (Fig. 27). It is important, because operating on the peak of the velocity curve provides stable drift velocity, and makes it insensitive to small pressure and temperature fluctuations. Low voltage provides the field cage design simplier.

Nearly perfect electric field is provided by an inner and an outer field cage and by a high voltage central membrane. These properties allow secondary electrons drift to the anode plane without any distortion in recorded tracks. Both cages also serve the purpose of determining the active gas volume, and

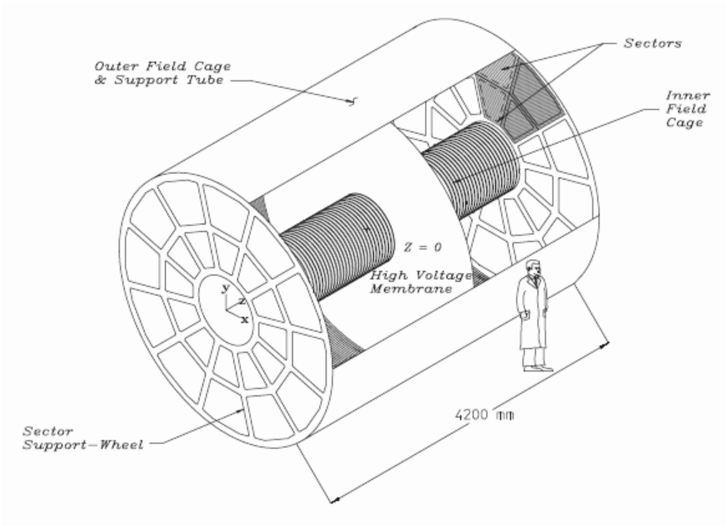

Figure 26: STAR TPC schema [57].

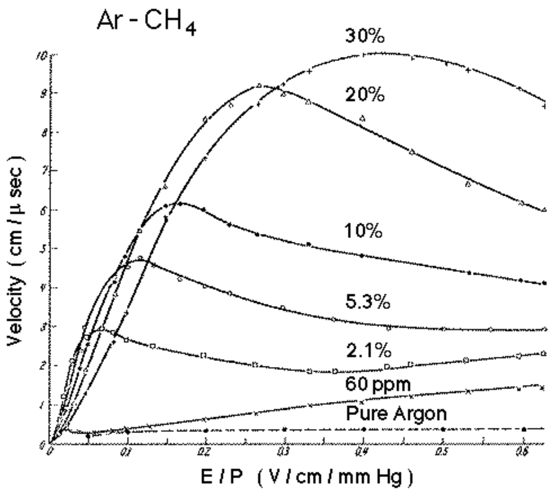

Figure 27: Electron drift velocity as a function of reduced electric field for different gas mixtures [57].

were designed in such a way as to prevent TPC gas from contamination by outside air. The mechanical design was optimized to reduce mass, minimize track distortions from multiple Coulomb scattering, and to reduce secondary particle production background [57].

In the middle of the TPC there is the central membrane located as shown in Fig. 26. This thin conductive membrane is under high voltage, and defines a uniform electric field required to drift electrons. The membrane is operated at 28 kV.

Pad planes are organized into sectors and are held at the ground potential. The space between the central membrane and the anode planes is divided by a series of gradient rings. Each ring is separated from the next one by a 2 Ω resistor, which provides a uniform gradient between the central membrane and the grounded endcaps. The readout endcap modules are split into 12 sectors around the beampipe. Each sector is divided into an outer and an inner sub-sector in the readout plane. In the inner sub-sector the density of tracks is higher, and therefore, pads are smaller than in the outer sub-sector. One of these sectors is figured in Fig. 28, where the inner sub-sector is on the right and the outer one on the left.

The x and y coordinates of the track are reconstructed from the pad signal. The z position is determined from the drift time of a cluster of secondary electrons from the point of origin to the endcaps and from the average drift velocity. The most important features of the STAR TPC are listed in Tab. 6.

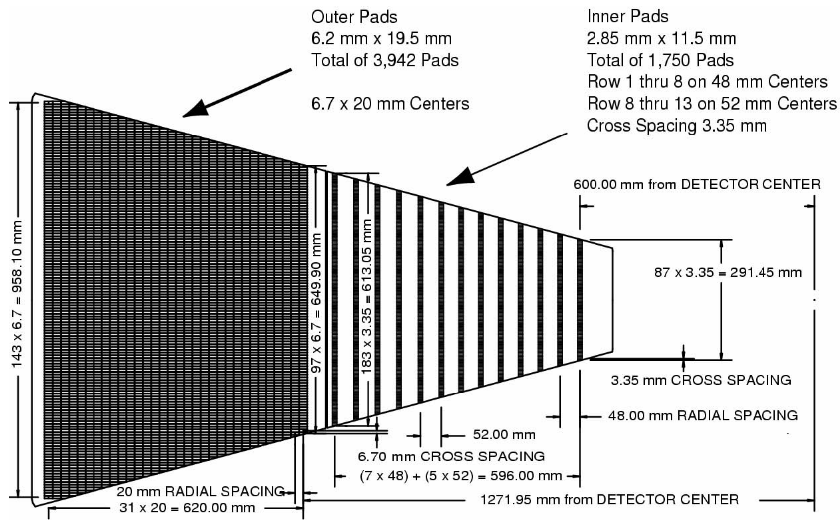

Figure 28: One sector of the readout endcap module. The inner sub-sector is on the right with small pads arranged in widely spaced rows. The outer sub-sector is on the left and is densely packed with larger pads [57].

Vertex resolution

If the vertex resolution is good enough, the primary vertex can be distinguished from the secondary vertices. As mentioned further, the primary vertex can be used to improve the transverse momentum resolution. The primary vertex can

Length	420 cm
Outer diameter	400 cm
Inner diameter	100 cm
Cathode potential	28 kV
Drift gas	P10 (10% methane + 90% argon)
Pressure	2 mbar above atmospheric pressure
Number of anode sectors	24 (12 per each end)
Number of pads	136608
Signal to bcg ratio	20:1
Drift Velocity	5.45 cmμs
Transverse Diffusion	230 μm/pcm 140 V/cm
Longitudinal Diffusion	360 μm/pcm 140 V/cm

Table 6: The most important features of the STAR TPC [57].

be found by extrapolating all tracks reconstructed in the TPC to the origin. Than the total average is considered the primary vertex position. The total average is calculated by comparing positions of vertices that are reconstructed using each endcap of the TPC separately. The resolution decreases with the square root of the number of tracks used in calculation. A resolution of 350 μm is achieved when there are more than 1000 tracks used in calculation. The primary vertex resolution as a function of the particle multiplicity is shown in Fig. 29.

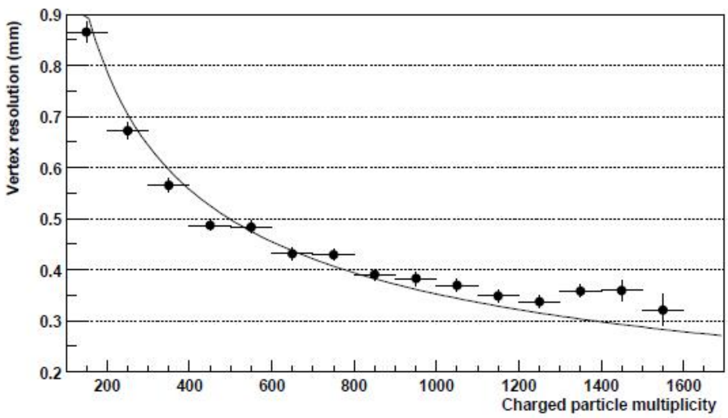

Figure 29: Primary vertex resolution in the transverse plane in Au+Au collisions at $\sqrt{s_{NN}}$ = 130 GeV [57].

Momentum resolution

Charged particle transverse momentum is solved by fitting a curve (in x and y coordinates) along the particle track. The total momentum is calculated from this radius and the angle that the track makes with respect to the Z axis. For all primary particles, this can be done with respect to the primary vertex; for secondary particles, the transverse momentum fitting must be done without this reference. That means that the transverse momentum resolution is lower for secondary particles than for primary particles.

The transverse momentum resolution of primary particles tracks fit through the primary vertex is shown in Fig. 30. For transverse momentum above 1 GeV/c, it is more difficult to resolve the curvature of the track. This means that the momentum relative error increases for high p_T. At low momenta, the resolution is affected by the energy loss in the TPC. Due to their smaller energy these low momentum particles lose a significant proportion of their energy in the TPC, do not travel through the whole volume in the TPC, and therefore their tracks are shorter. The momentum measurement error increases as a consequence. Finally, the energy loss in the TPC is dependent not only on the particle momentum, but also on the mass of the particle, so that there are differences in the resolution for different particles at low momenta, as figured in Fig. 30 for antiprotons and pions.

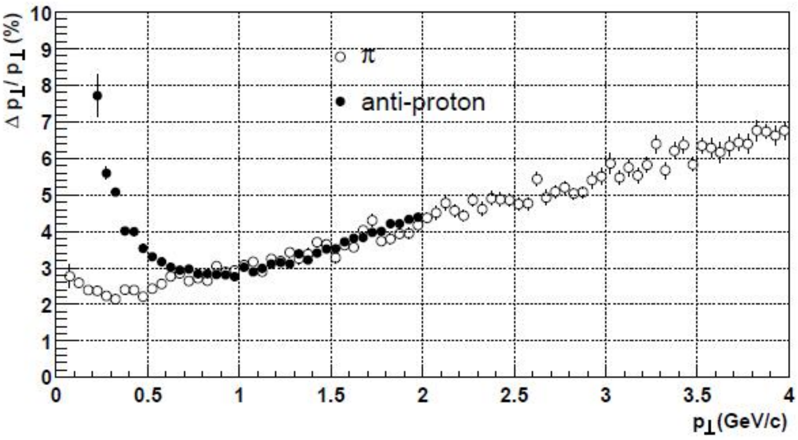

Figure 30: The transverse momentum resolution of the STAR TPC for π^-, and antiprotons in $Au + Au$ collisions at $\sqrt{s_{NN}} = 130$ GeV [57].

Particle identification through ionization energy loss

A charged particle that traverses the TPC volume ionizes gas atoms along its path and leaves clusters of electrons. These clusters of electrons drift to the anode plane where their positions and time of arrival are recorded. Trajectories of primary ionizing particles are reconstructed from these released secondary electrons. The ionization energy loss (dE/dx) is calculated from the energy loss measured on up to 45 pad rows, and it is a powerful device used to identify particles. The energy loss per unit length is described by the Bethe-Bloch formula [61]

$$-\frac{dE}{dx} = \frac{1}{4\pi\epsilon_0}\frac{z^2e^4}{m_ec^2}\frac{1}{\beta^2}\left[\ln\frac{2m_ec^2\beta^2}{I(1-\beta^2)} - \beta^2\right], \tag{21}$$

where m_e is the electron mass, z is the charge of the particle, ϵ is the free space permitivity, I is the mean excitation potential, and n is the particle density in the target. The ionization energy loss dE/dx as a function of particle momentum is shown in Fig. 31, where the dE/dx resolution is depicted by color bands.

Ionization fluctuations and finite track lengths limit the dE/dx particle identification. Based on the less mass-dependent energy loss for high momentum particles, the relative dE/dx resolution was established at 7% [57]. This resolution is achieved by requiring at least 20 of 45 hits in the TPC used for the track reconstruction. Only tracks satisfying this condition are accepted. Next to the number of hits recorded in the TPC, the dE/dx resolution depends on event multiplicity, beam luminosity, magnetic field settings, track length, and drift distance. The resolution improves with more hits in the TPC, stronger magnetic field, longer tracks, shorter drift distance, lower beam luminosity, and for lower multiplicity. Another uncertainties of the dE/dx measurement depend on the gas gain that itself depends on the pressure in the TPC, which varies with time. The gas gain is monitored by a wire chamber. The read out electronics also introduce inaccuracy in the dE/dx signal. Other uncertainties are generated due to different responses of readout boards, and there are also small variations between single pads.

6.4 Time of Flight and particle identification

The STAR particle identification capability could be enhanced by using the Time of Flight (TOF) information and the data from TPC together. It is a very useful improvement if electrons are identified by using dE/dx information from the TPC and velocity information from the TOF. It makes charm production measurement through a dielectron decay channel purer and more efficient.

While TPC is a strong tool for identification particles with higher p_T, the TOF detector is a powerful component for distinguishing low p_T particles. It can be seen from Fig. 31 and Fig. 32 that neither TPC nor TOF alone are able to distinguish charged hadrons in the intermediate p_T range, 2 GeV< p_T <4 GeV. However, the combination of both pieces of information provides good PID capability. With the combination of dE/dx information from the TPC and β

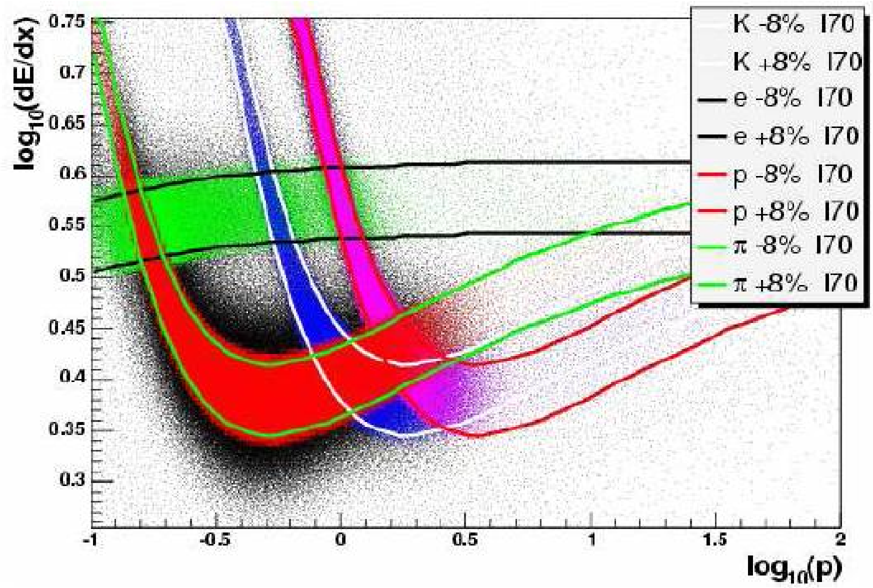

Figure 31: The dE/dx distribution as a function of momentum for electrons, pions, protons and Kaons. The dE/dx resolution is denoted by color bands [62].

from the TOF, electrons can be identified above $p_T > 0.15$ GeV/c, while the high p_T reach is limited by the statistics in analysis.

6.5 The Barrel Electromagnetic Calorimeter

The Barrel Electromagnetic Calorimeter (BEMC) is located inside the STAR solenoid and covers $|\eta| <1$ and the full azimuthal angle, thus matching the acceptance for full TPC tracking. The BEMC consists of 120 calorimeter modules, each of them segmented into 40 towers. Every tower is oriented to the direction of the interaction point. The inner surface of the BEMC has a radius of about 220 cm, and the outer radius is about 250 cm. In each module there are 21 active plastic and lead scintillating layers.

The calorimeter has a total depth of approximately twenty radiation lengths [63]. The BEMC provides a large acceptance for photons, electrons and π^0 mesons. All these measurements require precise electromagnetic shower reconstruction with a high spatial resolution. Hadrons typically deposit far less than their total energy in a tower. Due to this fact, E/p is a powerful electron identification tool.

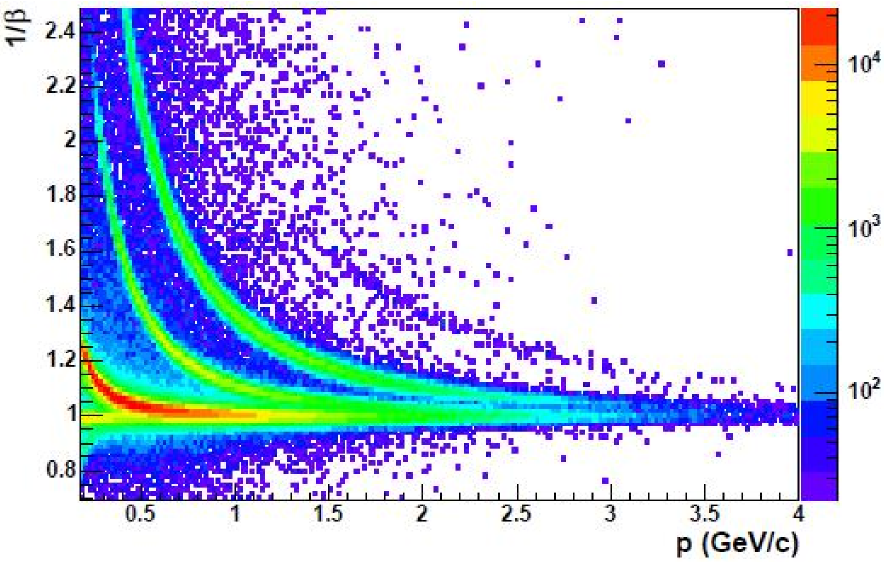

Figure 32: Value $1/\beta$ as a function of the momentum for pions, Kaons and protons from TOF at 62.4 GeV $Au + Au$ collisions. The visible separation between pions and kaons is reached for $p_T < 1.6$ GeV/c [62].

6.6 J/ψ trigger

The low-p_T J/ψ trigger consists of information from the BEMC, the CTB (the central trigger barrel, used during $p + p$ analysis in the year 2006), and since the year 2009 from the TOF detector (used on Au+Au data from the year 2010 [65]). It is used to electrons and positrons selection from the photon background. This is allowed because the CTB and the TOF are sensitive only to charged particles. The trigger without TOF does not provide sufficient background rejection because the granularity of the CTB is too rough [64]. The J/ψ low-p_T trigger was established with respect to the fact that low-p_T J/ψ decays into the di-electron pair with the large open-angle. The low-p_T J/ψ trigger consists of two steps. The first level L0 requires:

- at least two towers with $E_0 > 1.2\ GeV/c^2$
- the angular separation between towers mentioned previous at least $\theta \geq 60°$, where θ is calculated assuming interaction vertex at (0,0,0), and straight tracks approximation

These parameters were chosen base on simulations [64]. The second level L2 requires (with the CTB setup):

- signal in the CTB slat that corresponds to the chosen tower is requested, this requirement displaces towers that received their energy from photons

- a cluster energy required to be greater than chosen threshold, for this calculation 3 towers are used, the L0 tower plus 2 neighboring towers with the highest energy
- $2.2 < M < 5.0$ GeV/c^2 calculated from equation $M = \sqrt{2E_iE_j(1-\cos\theta)}$, where E_i and E_j are energies of the clusters i and j and θ is the open-angle between them

The second level L2 (TOF included) requires same second and third conditions and in addition it requires:

- at least one TOF hit matched to any tower in the cluster

If both levels are satisfied the event is recorded. The trigger capacity is determined by two factors - the background rejection and the signal efficiency. Therefore the trigger parameters must be established with respect to these opposite requirements. Must be strong enough to increase background rejection and soft enough to provide sufficient signal efficiency.

7 J/ψ reconstruction in $d + Au$ collisions at $\sqrt{s} = 200 GeV$ at the STAR

In this work, an analysis of J/ψ meson production in $d + Au$ collisions at $\sqrt{s_{NN}}$= 200 GeV using data taken during the 2008 run with the STAR experiment at BNL is presented. Author of this thesis participated at data taking in period 2009-2011 as detector operator. For this analysis STAR Libraries and STAR MuDst production of dAu (version SL10c) were used. These MuDst files were reduced to the ROOT Trees which contain particle trajectory information. As a part of this work, the programm for analysis of these ROOT files was created.

Selected events have the Z axis [1] component of the primary vertex [2] from -30 cm to 30 cm from the detector mid-point and taken with a minimum bias trigger [3]. The total number of Minimum Bias events and the number of events that passed through event cuts are listed in Tab. 7.

MinBias data	46 M
zVertex cut	32.5 M
$\mathrm{N_{BEMC}}$ cut	31 M

Table 7: Total number of events before any cuts and after events cuts.

Additional criterium required in this analysis $N_{BEMC} \geq 1$, where N_{BEMC} is the number of tracks matched to the hit in BEMC. This cut reduces the contribution of pile up events. Next event criterium used in this analysis is a pseudo-rapidity cut for reconstructed particles. Daughter electron or positron, whose pseudo-rapidity η is in the absolute value larger then 1, cannot be reconstructed in the TPC. Hence, only positrons and electrons with the pseudo-rapidity in the range $|\eta| < 1$ were accepted. The pseudo-rapidity distribution is shown in Fig. 33. The pseudo-rapidity distribution is centrally skew since asymmetry of $d + Au$ collisions. All used event cuts are listed in Tab. 8.

|zVertex|	< 30 cm
$\mathrm{N_{BEMC}}$	≥ 1
$\|\eta\|$	< 1 cm

Table 8: Summary of event cuts used in this analysis.

The reference multiplicity is a characteristic quantity of an event defined as a number of charged particle tracks well reconstructed at mid-rapidity $|\eta| < 0.5$. The reference multiplicity is related to the collision centrality. This could

[1] Z axis is that along the beam axis.

[2] The primary vertex is found by extrapolating all reconstructed tracks of charged particles to the origin and global average is given as the primary vertex position.

[3] The minimum bias trigger requires in the online regime the time difference between two signals from VPD detectors that corresponds to the $V_z < 30$ cm.

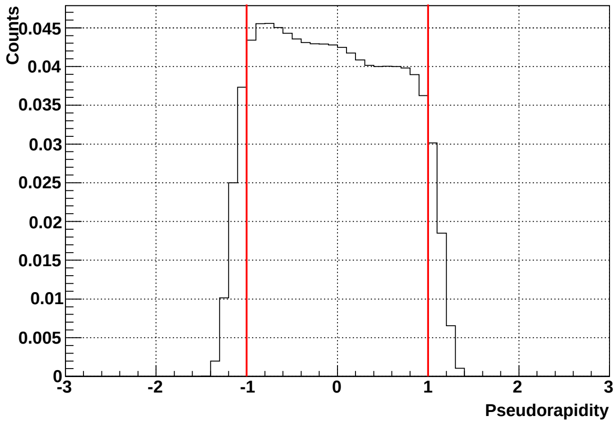

Figure 33: The pseudo-rapidity distribution of all charged particles. Red lines denote the used cut ($|\eta| < 1$).

be simulated within Glauber model. The Glauber model describes a nuclear collision as an ensemble of nucleon-nucleon collisions in the overlap region in a plane transversal to the beam line [66]. In this analysis, collisions have been divided into three centrality classes, $0-20\%$, $20-40\%$ and $40-100\%$ of the most central collisions. The multiplicity distribution is shown in Fig. 34.

The efficiency of the VPD detector is smaller for low multiplicity events. Due to this fact, there are significant differences between the real multiplicity distribution and the multiplicity obtained from the Glauber MC calculation for $40-100$ % central collisions. Therefore the multiplicity reweighting was done for this centrality class (the obtained reweighting factor ~ 2). For other centrality classes ($0-20$ and $20-40$ % of the most central collisions), the difference between real data and the Glauber MC calculation is negligible.

The mean number of participants and the number of binary collisions for each centrality class are listed in Tab. 9.

Centrality class	Multiplicity	$N_{\text{participants}}$	$N_{\text{collisions}}$
$0-20$	$M_{\text{reff}} > 10$	15.22	14.60
$20-40$	$6< M_{\text{reff}} \leq 10$	11.37	10.75
$40-100$	$M_{\text{reff}} \leq 6$	5.65	4.75

Table 9: Centrality definitions obtained from Glauber calculations using FTPC-E [11].

This chapter consists of two principal parts. First, the track selection is discussed, and than the electron identification is presented. These steps were done for all centrality classes together.

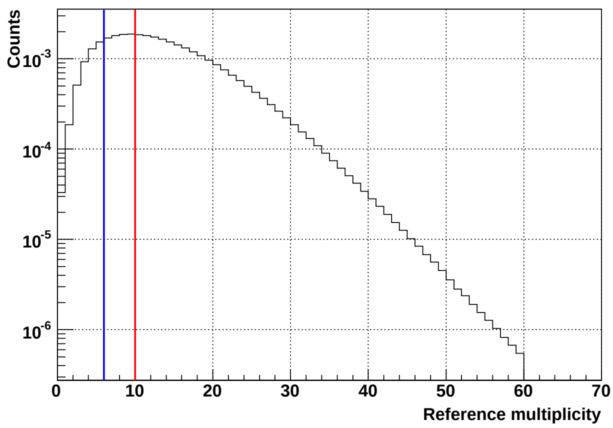

Figure 34: The multiplicity distribution. Blue and red lines divide centrality classes.

7.1 Track selection

Particle tracks were reconstructed from registered hits in the TPC readout system. The number of these fit points is the main criterium for a track selection quality. If only a few hits are associated with a track, they may give a arbitrary result. Only tracks reconstructed from more than 19 points were accepted ($N_{\mathrm{fit}} \geq 20$). For an elimination of double counting, another cut was used; the number of fit points over the number of maximum possible fit points is required to be $N_{\mathrm{fitmax}} > 0.51$. Both distributions ($N_{\mathrm{fit}}$ and N_{fitmax}) of all charged particles with denoted cuts are illustrated in Fig. 35 and Fig. 36 consequently.

In order to eliminate a contamination from secondary electron tracks, a global DCA cut ($gDCA < 2.0$ cm) was used. The $gDCA$ is a distance of a track to the global vertex of the event. The $gDCA$ distribution of all charged particles is shown in Fig. 37.

The J/ψ meson has large mass, therefore the produced electrons and positrons have typically larger momenta than the background. This difference in spectra is evident in momentum and transversal momentum distributions. The p_T distribution of all charged particles is shown in Fig. 38. Distributions of simulated J/ψ daughter electrons and positrons, p_T and p, are shown in Fig. 51 and Fig. 52 respectively. Hence, the transversal momentum cut was established as $p_T > 1.0$ GeV/c, and, in addition the momenta cut $p > 1.2$ GeV/c was used. The second reason for these cuts is a large hadron contamination for low p or p_T electrons and positrons sample. This contamination is visible in Fig. 39, where Bischel functions for electrons, pions, protons and kaons are illustrated. For charged particles with low p_T these functions cross each other. All track cuts used in this analysis are listed in Tab. 10.

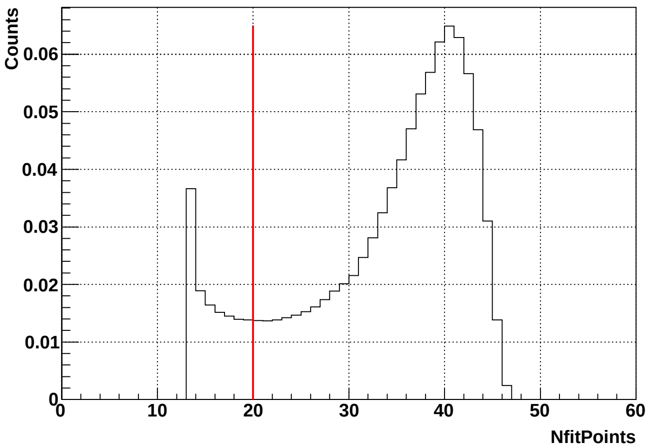

Figure 35: The N_{fit} points distribution of all charged particles. The red line denotes the used cut ($N_{\mathrm{fit}} \geq 20$).

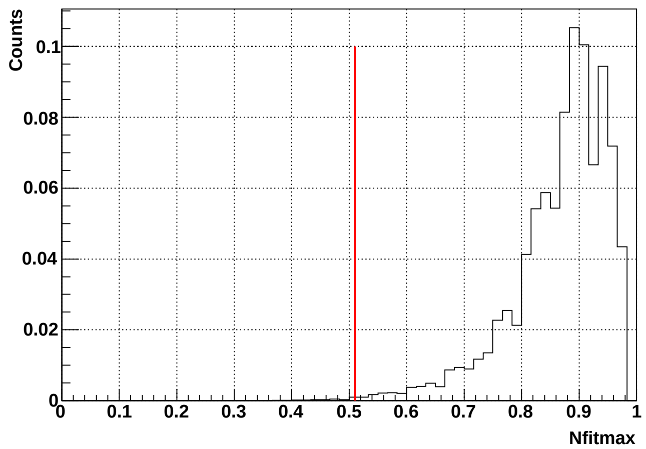

Figure 36: The N_{fitmax} distribution of all charged particles. Red line denotes used cut ($N_{\mathrm{fitmax}} > 0.51$).

7.2 Electron identification

In this analysis, the J/ψ signal is reconstructed from the electron-positron decay channel. Therefore the main part of the analysis is to identify electrons and positrons. A charged particle is usually identified through the mass-dependent ionization energy loss dE/dx that is measured in the TPC detector. Using

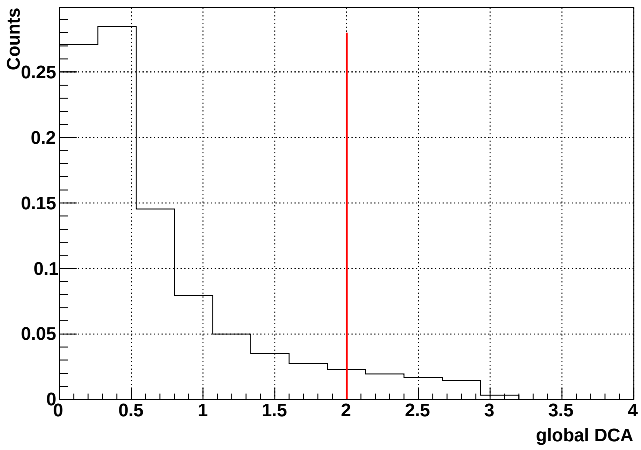

Figure 37: The $gDCA$ distribution of all charged particles. Red line denotes used cut ($gDCA > 2$ cm).

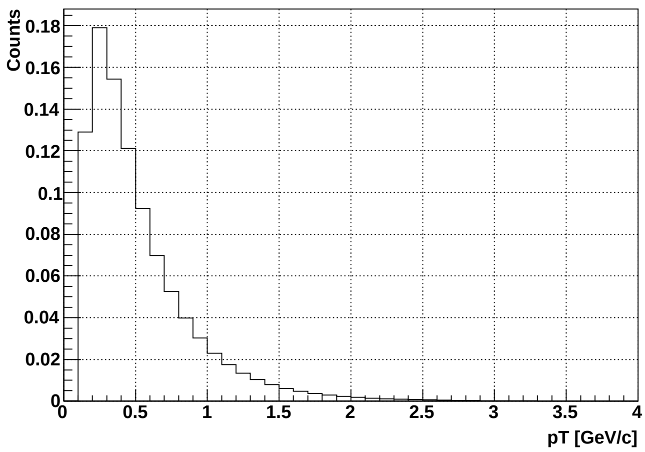

Figure 38: The p_T distribution of all charged particles.

the dE/dx information from the TPC, particles with a different mass can be distinguished. The distribution of dE/dx for all charged particles as a function of momentum is illustrated in Fig. 39.

To distinguishing electrons and positrons cuts based on a ionization loss were used. It is obvious from the electron ionization loss function that dE/dx for an electron is in the range $3 < dE/dx < 5$ keV/cm. Thanks to this fact and after some purity and efficiency tests, the dE/dx cut was established as

$N_{\rm fit}$	≥ 20
$N_{\rm fitmax}$	> 0.51
$gDCA$	< 2 cm
p_T	> 1.0 GeV/c
p	> 1.2 GeV/c

Table 10: The summary of track cuts used in J/ψ analysis in d+Au collisions at $\sqrt{s_{NN}} = 200$ GeV.

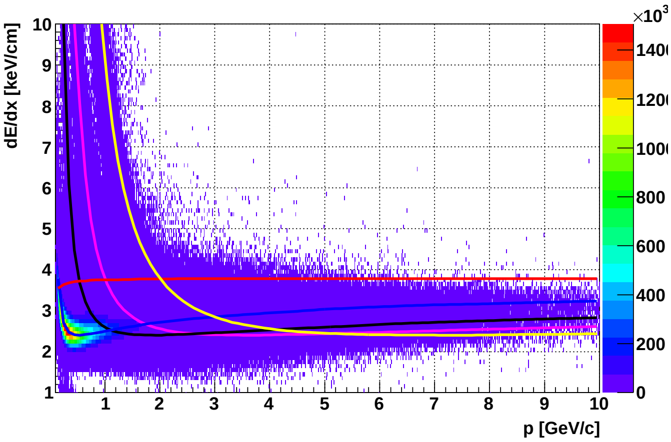

Figure 39: The dE/dx distribution of all charged particles as a function of the track momentum. Bichsel function lines for protons (violet), kaons (black), pions (blue), deuterons (yellow) and electrons (red) are shown.

3.2 < dE/dx < 4.85 keV/cm. Other quantity related with dE/dx is nsigma ($n\sigma$). It is defined as:

$$n\sigma_x = \ln\left(\frac{dE/dx_{\rm measured}}{dE/dx_{{\rm BetheBloch}_x}}\right)/\sigma, \quad (22)$$

where dE/dx$_{\rm measured}$ is a measured ionization loss, dE/dx$_{{\rm BetheBloch}_x}$ is a ionization loss of the particle x from BetheBloch function, where x means a proton or a pion and σ is error associated with dE/dx measurement. For the STAR TPC detector we have $\sigma = 0.075$ [67]. This quantity can be calculated for electrons as well, but it is evident from the electron Bischel function that previously mentioned dE/dx cut is identical. In this analysis, $n\sigma_{pion}$ and $n\sigma_{proton}$ cuts were used to obtain the final lepton sample with a low hadronic contamination. All these TPC cuts are summarized in Tab. 11. The dE/dx distribution as a function of the momenta after event cuts, track quality cuts and these electron identification cuts are shown in Fig. 40, where Bischel functions for pion, proton, electron, kaon and deuteron are represented by solid lines. The background on the right from the electron gaussian curve originates from deuterons and that on the left from the pion curve originates from Kaons as is saw in Fig. 39.

$\lvert n\sigma_{proton}\rvert$	> 2.2
$\lvert n\sigma_{pion}\rvert$	> 2.5
dE/dx	$3.2 < dE/dx < 4.85$ keV/cm

Table 11: The summary of electron identification cuts used in J/ψ analysis in $d + Au$ collisions at $\sqrt{s_{NN}} = 200$ GeV.

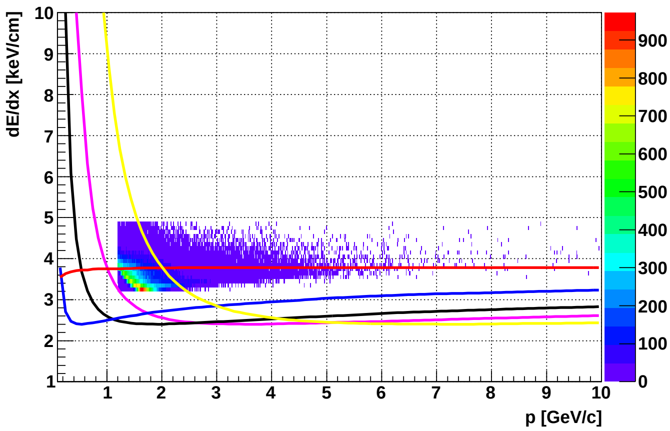

Figure 40: The dE/dx distribution of charged particles that passed track quality, and TPC cuts as a function of the track momentum. Bichsel function lines for protons (violet), kaons (black), pions (blue), deuterons (yellow) and electrons (red) are shown.

Examples of the dE/dx distribution of all charged particles that passed track quality cuts are shown in Fig. 41 and Fig. 42. These distributions are used for establish the electron identification efficiency, which is discussed in the next chapter.

An electron can be identified with the both TPC and BEMC, this reduces hadron contamination. Trajectories of electron candidates are extrapolated to BEMC towers. In the BEMC, particles deposit specific amount of their kinetic energy depending on type of the partical. Electrons deposit almost all their energy via electro-magnetic showers there, while hadrons deposit only its small part. The energy of the corresponding tower is used to compute the ratio with its corresponding track momentum, p/E. Considering this fact and the ultra-relativistic state of electrons, p/E must be approximately equal to one. Then the p/E cut $(0 < p/E < 2)$ can select most electrons, and reject a large amount of hadrons. Finally, due to the better purity-efficiency ratio, only the TPC cuts

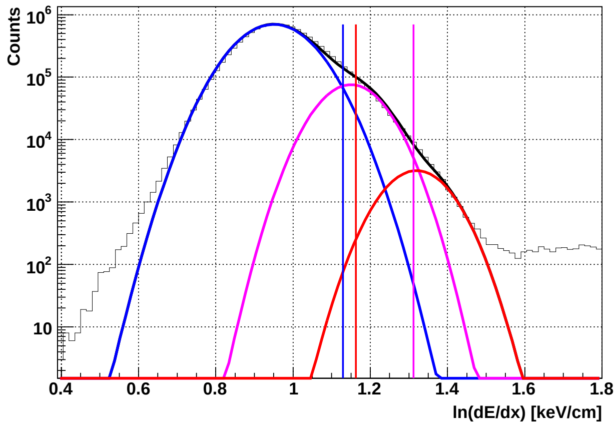

Figure 41: The dE/dx distribution for all charged particles that passed track quality cuts with $1.2 < p_T < 1.3$ GeV/c. Gaussians show pion (blue), proton (violet) and electron (red) yields. The accepted electrons are those on the right side from the violet solid line that denotes the nσ_{proton} cut.

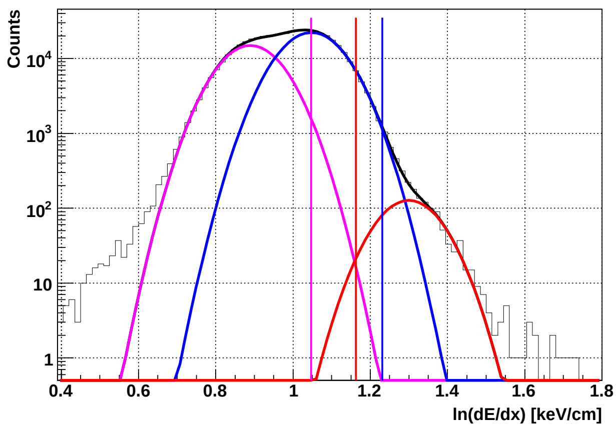

Figure 42: The dE/dx distribution for all charged particles that passed track quality cuts with $2.8 < p_T < 3.0$ GeV/c. Gaussians show pion (blue), proton (violet) and electron (red) yields. The accepted electrons are that on the right from the violet solid line that denotes nσ_{pion} cut.

were used in this analysis.

7.3 The raw J/ψ spectrum

The J/ψ signal in the e^+e^- decay channel is identified as a prominent peak in the dielectron invariant mass spectrum M_{inv} is defined as:

$$M_{inv} = \sqrt{(E_+ + E_-) - (p_+ + p_-)}, \tag{23}$$

where E_+, E_-, p_+, and p_- are positron energy, electron energy, positron momentum, and electron momentum respectively. Since J/ψ has a large mass and consequently daughter electrons and positrons must have large momentum and energy it was used approximation $m_ele = 0$ for invariant mass calculation:

$$M_{inv} = 2sin(\frac{\theta}{2})\sqrt{p_+p_-}, \tag{24}$$

where p_+ and p_- are the positron and the electron momenta, and θ is the open angle between the electron and the positron. Since $M_{J/\psi} = 3.097$ GeV/c^2, the estimated peak region is $3.0 < M_{J/\psi} < 3.2$ GeV/c^2. In every event, many dielectron candidates can be reconstructed. Only some of them are J/ψ or other decays signals, other combinations are random. These random combinations are called the combinatorial background (N_{bg}). In this analysis, the geometric mean N_{bgg} background was calculated. The N_{bgg} is estimated from like-signed pairs (N_{--}, N_{++}) as follows:

$$N_{bgg} = \sqrt{N_{++}N_{--}}, \tag{25}$$

the J/ψ signal is defined as follows:

$$N_{J/\psi} = N_{tot} - N_{bgg}, \tag{26}$$

and the significance of the final J/ψ signal is defined as:

$$sg = \frac{S}{\sqrt{S + 2B}}, \tag{27}$$

where S is the J/ψ signal after background subtraction, B is the background and $B + S$ is the total yield of e^+e^- pairs.

Dielectron invariant mass distributions in $d + Au$ at $\sqrt{s_{NN}} = 200$ GeV collisions before and after background subtraction are shown in Fig. 43 and Fig. 44 consequently. The significance of the J/ψ signal and the final signal size for all centrality were estimated at ($sg = 4.9\sigma; S = 58$). The signal was fitted with a gaussian function. The mean and the sigma of the gaussian fit were found to be (3.11; 0.045) GeV. Another way how to fit the J/ψ signal is a fit with a Crystal Ball function. In this analysis, we fit with gaussian function.

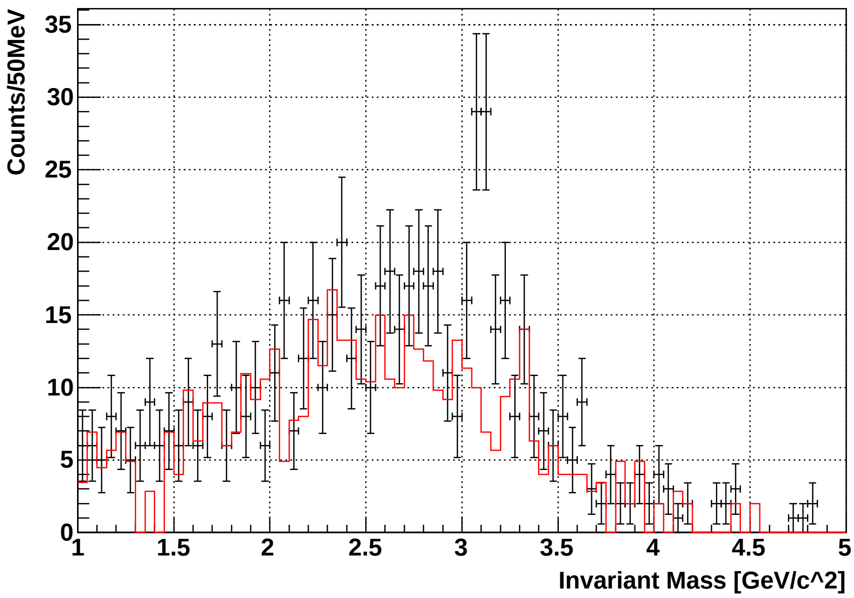

Figure 43: The uncorrected J/ψ invariant mass spectrum before background subtraction, where red line denotes the combinatorial background.

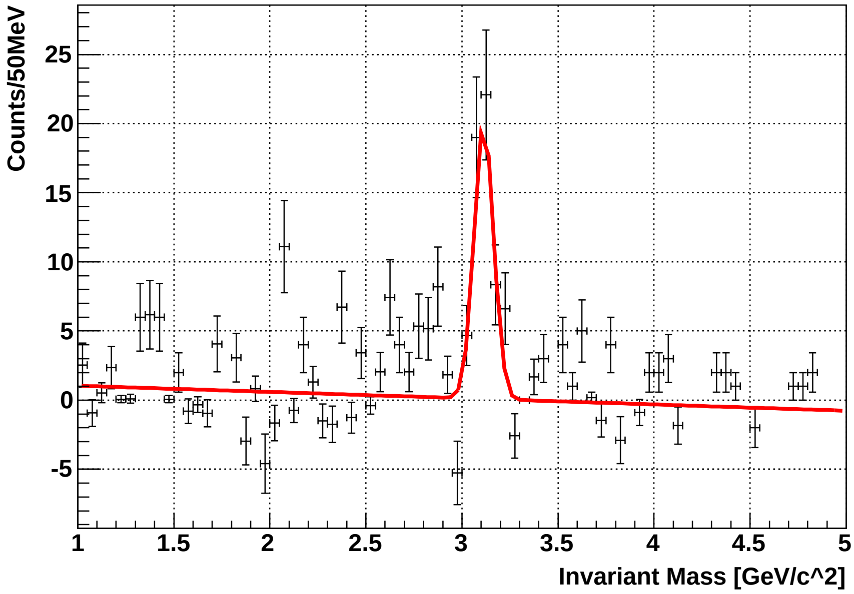

Figure 44: The uncorrected J/ψ invariant mass spectrum after background subtraction, where red line denotes fitted peak of J/ψ and the residual background. The significance is 4.9σ, and the signal S=58. The J/ψ peak is fitted with a gaussian fit with the mean and the sigma found to be (3.11; 0.045) GeV.

8 Acceptance and efficiency

Due to limited acceptance and efficiency not all J/ψ mesons created in a single collision could be reconstructed. To obtain the real number of produced J/ψs, the raw yield of J/ψs need to be corrected. The correction factors could depend on p_T spectrum of J/ψ and pseudorapidity and are extracted from simulations.

8.1 J/ψ reconstruction efficiency

The J/ψ reconstruction efficiency, including the detector acceptance and the track reconstruction efficiency is determined from the reconstruction of Monte Carlo simulated J/ψ's embedded into real events. The total number of events used in the embedding was 95k. Simulated J/ψ's were generated with a flat transversal momentum distribution (Fig. 45, $p_T 0-5$ GeV), and they are embedded into real events. Number of embedded J/ψ in each event was equal to 1. On analysis of simulated data it is possible to relate parent J/ψ and decay products by Geant ID information. The generated flat p_T spectrum was re-scaled by a scale function

$$f_{scale}(p_T) = 5.65 * 10^{-7} \left(1 + \left(\frac{p_T}{4.3}\right)^2\right)^{-6}, \tag{28}$$

that is power-law function fitted to the PHENIX data [53].

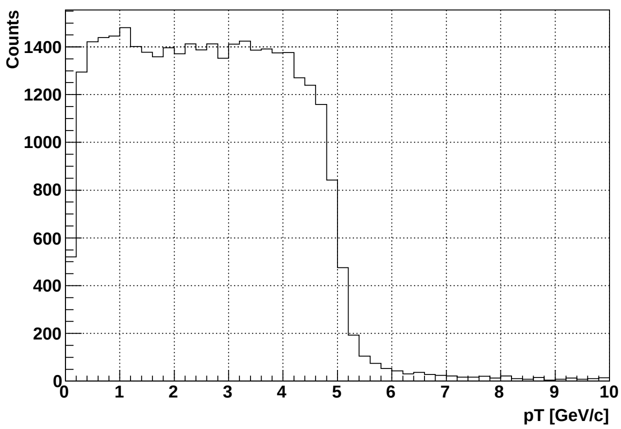

Figure 45: The simulated J/ψs p_T distribution before any cut.

Before determination of the detector acceptance and the track efficiency the event selection of simulated data was done. Only events with $|Z| < 30$ cm and events which the number of tracks matched to the BEMC $N_{BEMC} \geq 1$ were accepted in this analysis, therefore the same requirement is requested for simulation tracks. The zVertex distribution is shown in Fig. 46.

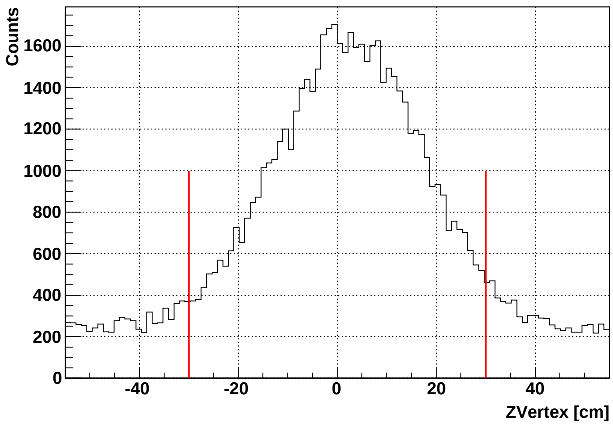

Figure 46: The zVertex distribution, red lines denote the zVertex cut.

Next the detector acceptance ϵ_{acc} will be discussed. In this analysis, the STAR detector acceptance is evaluated by a pseudo-rapidity cut. Daughter electrons or positrons, whose pseudo-rapidity η is in the absolute value larger then 1, cannot be reconstructed in the TPC, nor their mother J/ψ's can be found. The detector acceptance is defined as a fraction of electrons and positrons that complies with the pseudo-rapidity cut divided by the total number of electrons and positrons. Pseudorapidity distribution of electron and positrons is shown in Fig. 47.

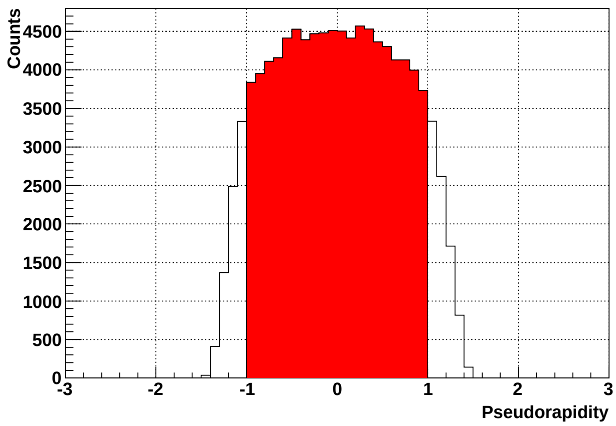

Figure 47: Pseudorapidity distribution of electrons and positrons, the red area represents electrons and positrons from J/ψ mesons that passed η cut.

The next step is an estimation of the track quality cuts efficiency. Track cuts, that means all cuts used in this analysis except the event cuts mentioned before, the dE/dx cut and $n\sigma$ cuts, were applied to embedded tracks to obtain a track efficiency correction factor. These cuts are summarized in Table 12.

$N_{\rm fit}$	≥ 20
$N_{\rm fit}/N_{\rm fitmax}$	> 0.51
$gDCA$	< 2 cm
p_T	> 1.0 GeV/c
p	> 1.2 GeV/c

Table 12: Summary of track quality cuts used for the estimation of the track quality cut efficiency.

Single distributions of daughter electrons and positrons values used for the track quality estimation $N_{\rm fit}$, $N_{\rm fitmax}$ and the global DCA with marked cuts are shown in Fig. 89, Fig. 90 and Fig. 50, respectively. The distribution of daughter electrons and positrons momentum and transversal momentum are shown in Fig. 52 and Fig. 51 respectively. Compared to the p_T distribution of all charged particles (Fig. 38), daughter electrons and positrons have a significantly larger momentum.

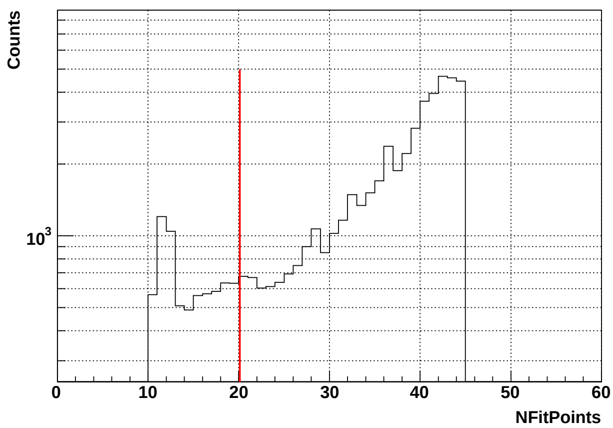

Figure 48: The TPC fit points distribution of all electrons and positrons used to the establish the track reconstruction efficiency. The red line denotes the selection cut $N_{\rm fit} > 20$.

Reconstructed electrons and positrons from simulated J/ψ's that passed the track quality cuts were identified and used to reconstruct the original parents, J/ψ mesons. The track reconstruction efficiency is defined as a number of reconstructed J/ψ's that satisfied the quality cuts divided by the total number

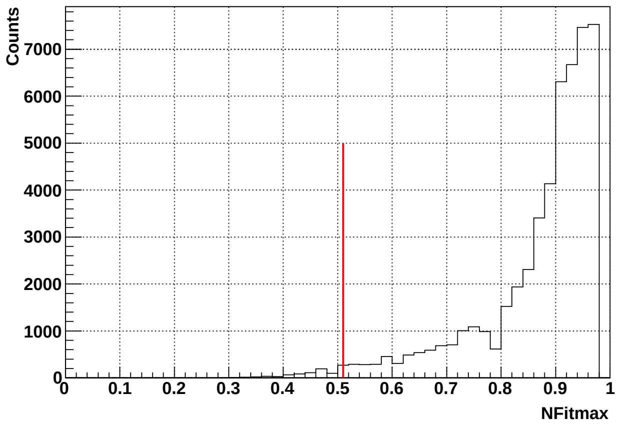

Figure 49: The N_{fitmax} distribution of all electrons and positrons used to the establish the track reconstruction efficiency. The red line denotes the selection cut $N_{\text{fitmax}} > 0.51$.

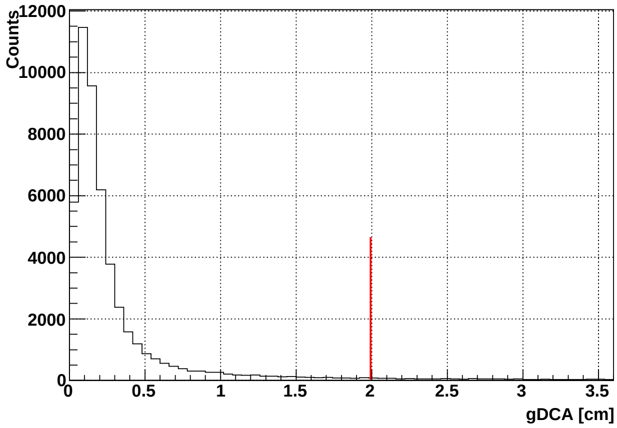

Figure 50: The gDCA distribution, red line denotes gDCA cut (gDCA < 2).

of embedded J/ψ's as a function of the transverse momentum. The total J/ψ reconstruction efficiency including detector acceptance, track quality efficiency and event selection efficiency was calculated like a convolution

$$\epsilon_{rec} = \epsilon_{acc} * \epsilon_{event} * \epsilon_{track}. \tag{29}$$

It is shown in Fig. 53 as a function of p_T of parent J/ψ.

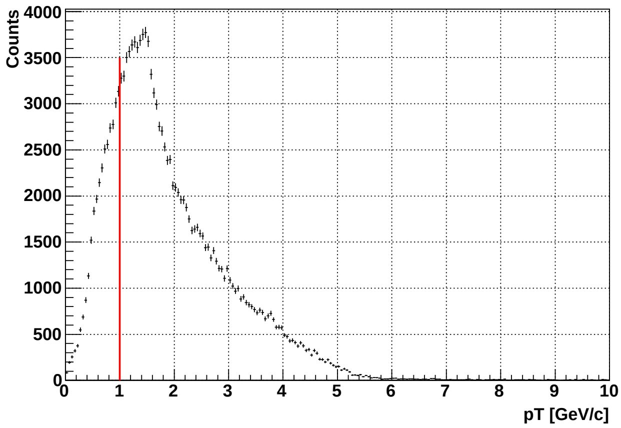

Figure 51: The electrons and positrons p_T distribution used in establishing the track efficiency. The red line denotes the selection cut $p_T > 1$ GeV.

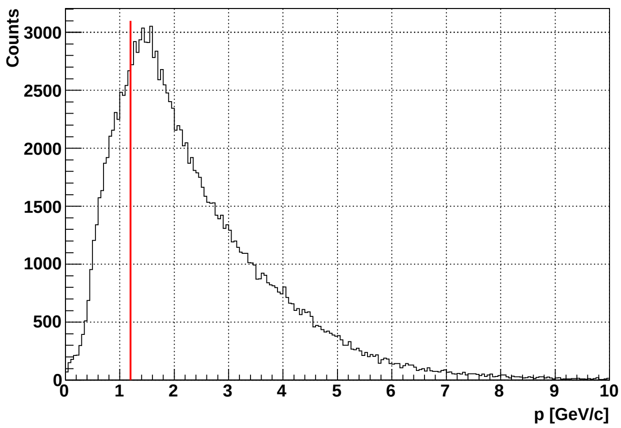

Figure 52: The electrons and positrons momentum distribution used in establishing the track efficiency. The red line denotes the selection cut $p > 1.2$ GeV.

8.2 Electron identification efficiency

In this section the electron PID efficiency will be discussed. The electron identification efficiency was defined as a fraction of electrons that passed through event cuts, track quality cuts and also through electron identification cuts, and all electrons produced in the collisions that passed through both track and event cuts. The total number of electrons reconstructed in the TPC was calculated by performing a multiple gaussian fit to the dE/dx distribution in dif-

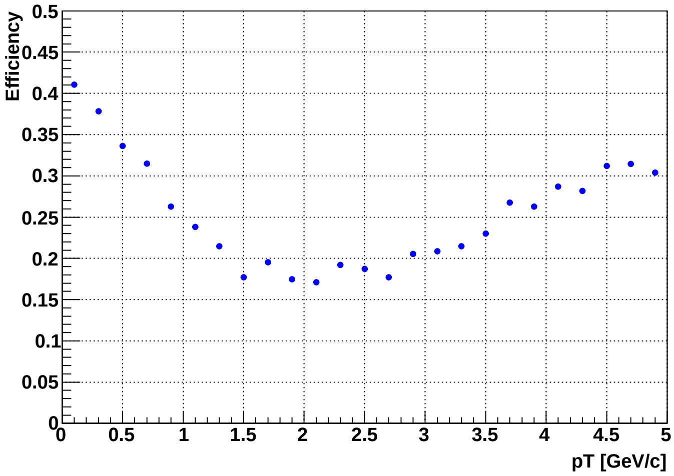

Figure 53: The J/ψ reconstruction efficiency.

ferent transversal momentum bins (bin width is 0.1 GeV/c for p_T smaller than 2 GeV/c and 0.2 GeV/c for larger p_T). Real data were used in this part of the efficiency calculation, because the estimation of the electron PID efficiency from embedded data is indeterminate. Electron PID cuts used in this analysis are summarized in Table 13.

$\|n\sigma_{proton}\|$	> 2.2
$\|n\sigma_{pion}\|$	> 2.5
dE/dx	$3.2 < dE/dx < 4.85$

Table 13: Summary of electron PID cuts used for the estimation of the electron identification efficiency.

The gaussian fit was determined with respect to the Bethe-Bloch functions for pion, proton and electron. Examples of gaussian fit to the dE/dx distribution for two different p_T bins were shown in Fig. 41 and Fig. 42 in Chapter 7.2, where the blue gaussian function displays the pion production, the violet one displays the proton production, and the red one shows the electron production. Solid lines show dE/dx and sigma cuts.

The final electron PID efficiency for single transversal momentum bins are shown in Fig. 54. The total acceptance and efficiency factor is estimated as

$$\epsilon_{total} = \epsilon_{rec} * \epsilon_{PID1} * \epsilon_{PID2}, \tag{30}$$

where ϵ_{PID1} and ϵ_{PID2} are daughter particles corresponding to the mother J/ψ with determined transversal momentum. Finally, this factor will be applied to

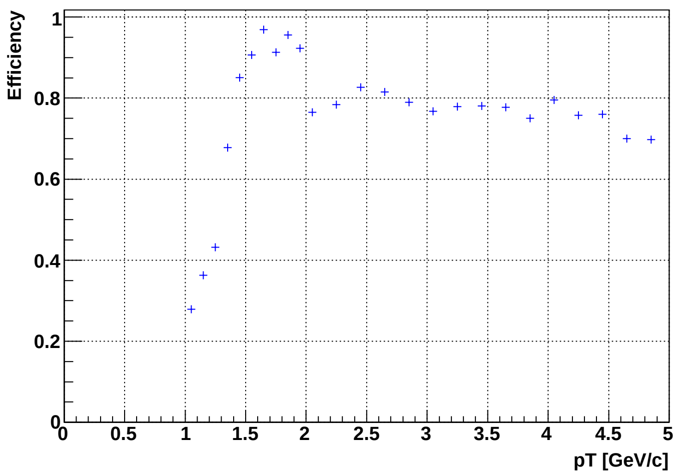

Figure 54: Electron PID efficiency as a function of electron transversal momentum.

the raw J/ψ p_T spectrum. The total efficiency as a function of J/ψ transversal momentum is shown in Fig. 55, where red marks denote the total efficiency, and blue marks show J/ψ reconstruction efficiency only.

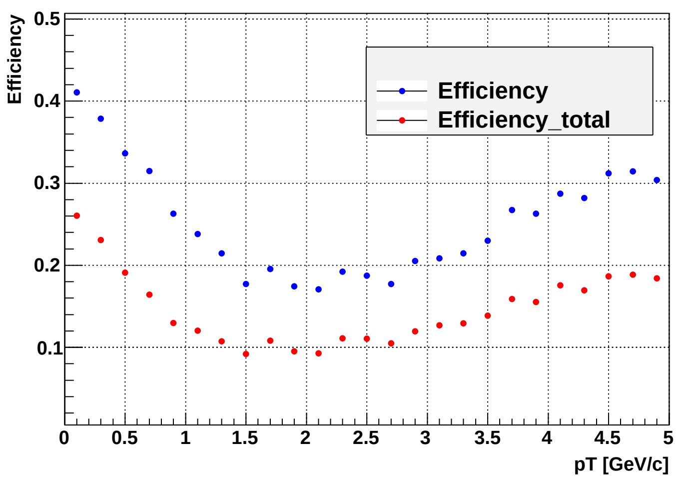

Figure 55: The total efficiency as a function of J/ψ transversal momentum. Blue marks denote J/ψ reconstruction efficiency, and red marks denote total efficiency including electron PID efficiency.

9 Systematic errors

Dominant sources of the systematic error, the electron PID efficiency uncertainty, the background subtraction error, the track reconstruction efficiency discrepancy, and the normalization uncertainty will be discussed bellow.

9.1 The electron PID efficiency uncertainty

The dE/dx efficiency uncertainty has two different origins, an error associated with gaussian fit to the dE/dx distribution, and the uncertainty of the method used for the electrons sample selection.

As mentioned above, the electron PID efficiency is defined as a fraction of electrons that passed through event cuts, track quality cuts and also through electron identification cuts, and all electrons produced in the collision that passed track and event cuts. Consequently, the electron PID efficiency depends on the accuracy that the number of electrons reconstructed in the TPC was calculated with. Calculations of the number of electrons were done by performing a multiple gaussian fit to the dE/dx distribution in different transversal momentum bins, where the gaussian fit was determined with respect to Bethe-Bloch functions for pion, proton and electron (Fig. 41 and Fig. 42 in Chapter 7.2).

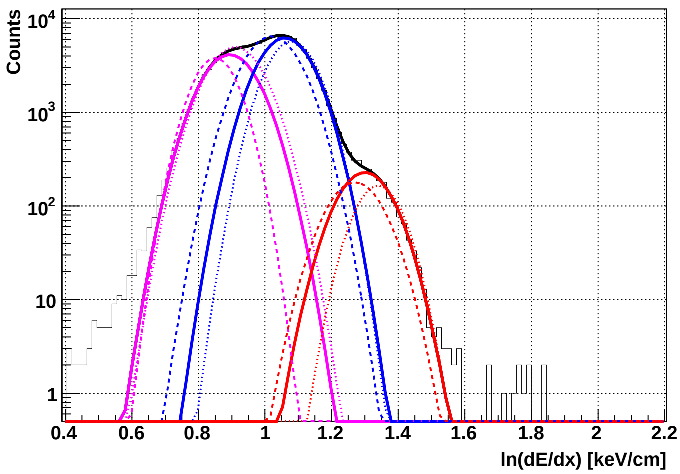

Figure 56: The dE/dx distribution for all charged particles that passed track quality cuts with $3.0 < p_T < 3.2$ GeV/c. Solid gaussian curves show primary results of pion (blue), proton (violet) and electron (red) yields. Dashed and dotted lines denote pion, proton and electron yields after the fit parameters shift. Parameters were shifted by $\pm$ one standard deviation for each particle spacies. The electron PID efficiency uncertainty in this p_T bin is 2.5%.

Since the electron PID efficiency is a function of gaussian parameters, the uncertainty of the electron PID efficiency was determined by shifting the gaussian parameters for each particle by one standard deviation of the fit results for each p_T bin, and looking at the effect on the electron dE/dx identification efficiency. The example of the parameter shift is shown in Fig. 56 for p_T bin $3.0-3.2$ GeV/c, where the solid lines denote the primary results, and the dotted and dashed lines show results obtained by parameter shifts. The uncertainty was established as $\sim 1.7\%$.

The second source of the electron PID efficiency error originates from the difference between the number of electrons obtained by performing a multiple gaussian fit to the dE/dx distribution and the number of electrons that passed through PID cuts (Tab. 11). The difference is illustrated in Fig. 57, where gray areas denote electrons that passed through electron PID cuts, but were not used for the electron PID efficiency calculation. The uncertainty was calculated for each p_T bin separately and averaged as $\sim 5\%$.

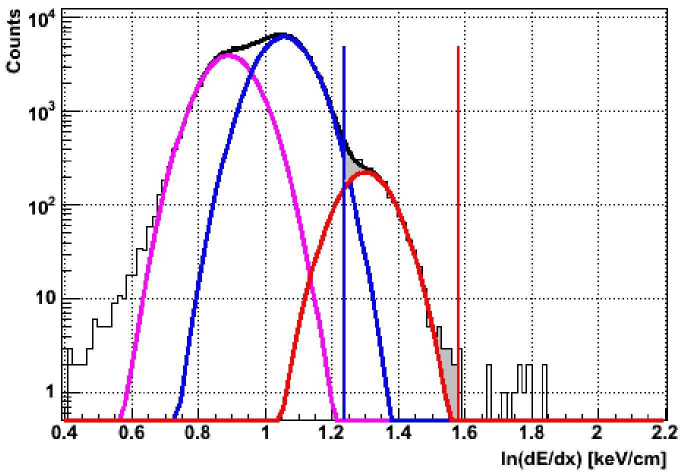

Figure 57: The dE/dx distribution for all charged particles that passed track quality cuts with $3.0 < p_T < 3.2$ GeV/c. Gaussian curves show primary results of pion (blue), proton (violet) and electron (red) yields. Grey areas show electrons passed through PID cuts that are not calculated for electron PID efficiency.

Finally, the total electron PID efficiency error was calculated by assuming both sources for both daughter particles.

9.2 The error associated with background subtraction

Background was calculated by a like-sign pair geometric mean method. As mentioned above, other methods for background reconstruction could be used. The uncertainty in a background calculation was determined by comparing the

J/ψ yield obtained using different background calculation methods, the like-sign arithmetic mean calculation, and the 4th order polynomial fit to the data except the J/ψ mass region $3.0 < M_{J/\psi} < 3.2$ GeV/c^2. The comparison between the geometric and the arithmetic mean like-sign pair methods is shown in Fig. 58, where the red line denotes the primary result of geometric mean background and the blue line shows comparative arithmetic mean background. The uncertainty was established as $\sim 2\%$. The collation between the geometric mean background and the 4th order polynomial fit is shows in Fig. 59. The uncertainty in this case was calculated as $\sim 5\%$. For the final calculation, the larger error was used.

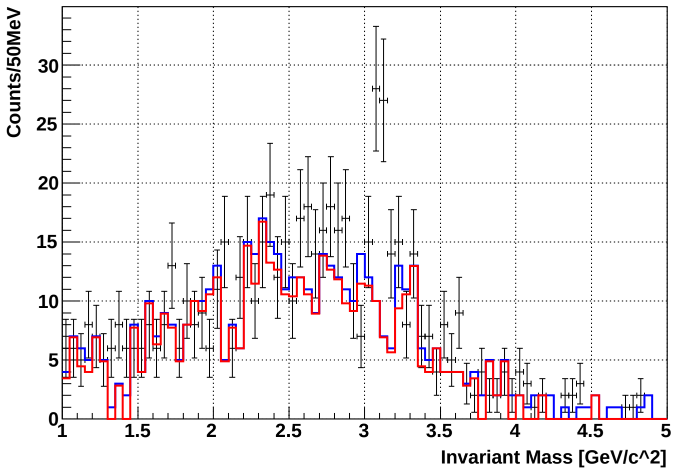

Figure 58: The J/ψ invariant mass spectrum, where the red line denotes geometric mean like-sign background, and the blue line shows arithmetic mean like-sign background. The uncertainty was calculated as $\sim 2\%$.

9.3 Track reconstruction efficiency uncertainties

The tracking efficiency of the TPC is determined from reconstruction of Monte Carlo simulated J/ψs embedded into real events. The tracking efficiency uncertainty was established by comparing the N_{fit} distribution in embedding and real data. The comparison between real and simulated distributions is shown in Fig. 60. The track reconstruction efficiency error was established as $\sigma_{track} \sim 5\%$. This contribution to the total uncertainty must be calculated twice, for both daughter electrons. Assuming a full correlation between daughter tracking efficiencies, the error is $\sigma_{track} \sim 10\%$.

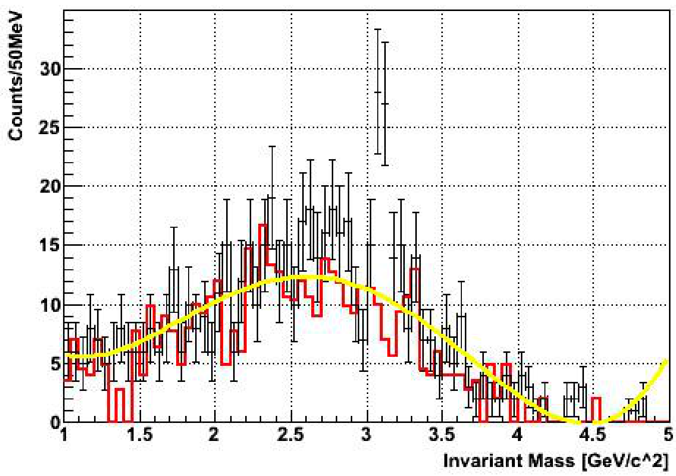

Figure 59: The J/ψ invariant mass spectrum, where the red line denotes geometric mean like-sign background, and the yellow line shows background calculated by the 4th order polynomial fit to the data. The uncertainty was calculated as $\sim 5\%$.

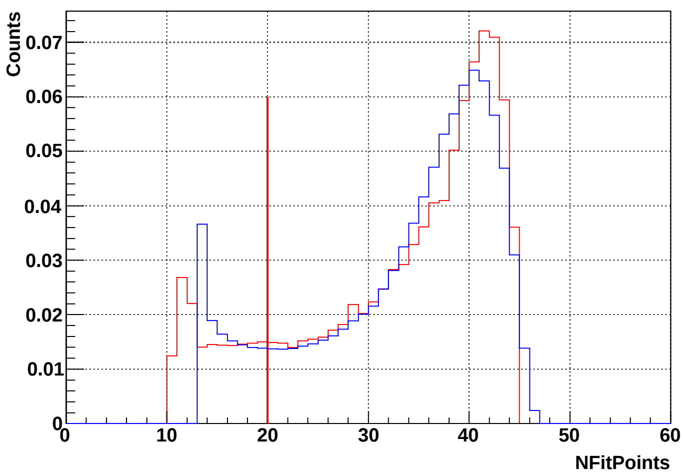

Figure 60: The N_{fit} distributions in embedding (red) and real data (blue).

9.4 Yield extraction uncertainties

As mentioned in Chapter 7.3, the yield was obtained by subtracting geometric mean like-sign background from the electron-positron mass spectrum. The obtained peak was fitted by the gaussian function, and the integral of the fitted histogram was used as a raw yield. The yield extraction uncertainty was calculated as a difference between raw spectra peak shape and simulated J/ψ spectra peak shape. For all centralities together, the error of the yield extraction was established as $\sim 32\%$. Than this comparison was done for each centrality bin separately, and the error in $20-40$ and $40-100\%$ bins became negligible, while the yield extraction uncertainty for most central collisions remained $\sim 33\%$. The error discrepancy between centrality bins was taken into account in the final calculation; hence, the total error for semi-central and peripheral collisions is significantly lower.

9.5 The normalization uncertainty

The nuclear modification factor R_{dA} was calculated by normalizing the invariant yield in $d+Au$ collisions to the yield in $p+p$ collisions, and scaled by the mean number of binary collisions in each centrality bin, as listed in Tab. 9. Hence, the uncertainty in the J/ψ $p+p$ yield must be considered. The J/ψ yield in $p+p$ collisions can be evaluated as

$$\frac{dN_{p+p}^{J/\psi}}{dy} = \frac{\sigma_{p+p}^{J/\psi}}{\sigma_{inel}}, \tag{31}$$

where the inelastic cross section is $\sigma_{inel} = 42 \pm 3$ mb, and the J/ψ cross section in $p+p$ collisions is $\sigma_{p+p}^{J/\psi} = 57 \pm 10\ (stat.) \pm 9\ (syst)$ nb [68]. From here, the normalization uncertainty of 21% was obtained.

Finally, the total error of the J/ψ invariant yield was calculated as

$$\sigma_{J/\psi} = \sqrt{\sigma_{PID}^2 + \sigma_{track}^2 + \sigma_{bcg}^2 + \sigma_{yield}^2}, \tag{32}$$

and for the most central collisions were evaluated as $\sigma_{J/\psi}^{centr} \sim 30.6\ \%$ while for the semi-central and the peripheral collisions $\sigma_{J/\psi}^{per} \sim 12.5\ \%$. The normalization uncertainty was kept separately.

10 Results

In this chapter, results obtained in J/ψ meson production in $d + Au$ collisions at $\sqrt{s_{NN}} = 200$ GeV using data taken during the year 2008 run of the STAR experiment at BNL are presented.

10.1 Corrected J/ψ p_T spectrum

The invariant mass was reconstructed for each p_T bin of width 1 GeV/c . Only the last bin has a width 2 GeV/c due to the small statistics. The invariant yield was calculated from the equation

$$\frac{\beta_{ee}}{2\pi p_T}\frac{d^2N}{dp_T dy} = \frac{1}{2\pi p_T}\frac{1}{\Delta p_T}\frac{1}{\Delta y}\frac{N_{J/\psi}}{N_{\mathrm{event}}}\frac{1}{\epsilon_{\mathrm{total}}}, \tag{33}$$

where $\epsilon_{\mathrm{total}}$ is the total efficiency presented in Chapter 8, $N_{J/\psi}$ is the number of reconstructed J/ψs, N_{events} is the total number of collisions, Δp_T is the p_T coverage ($\Delta p_T = 1$ for 0-1, 1-2, and 2-3 GeV/c bins, and $\Delta p_T = 2$ for 3-5 GeV/c bin), and $\Delta y = 2$. Number of reconstructed J/ψ's, significance and invariant yield for each p_T bin are listed in Tab. 14. Invariant mass spectra for each p_T bin are listed in Appendix C.

p_T [Gev/c]	$N_{J/\psi}$	Significance	Yield
0-1	29.6	2.5	$4.92 * 10^{-7}$
1-2	28.5	2.9	$3.28 * 10^{-7}$
2-3	18.0	3.5	$1.13 * 10^{-7}$
3-5	10.0	3.2	$1.35 * 10^{-8}$

Table 14: Number of J/ψ's reconstructed in each p_T bin, significance and invariant yield.

The corrected J/ψ p_T spectrum is shown in Fig. 61, where red marks show results obtained in this analysis, blue marks denote results obtained from an independent analysis [54], and the dotted line is a power-law fit to PHENIX data. The fitted function has the form

$$f(p_T) \sim A(1 + \frac{{p_T}^2}{B})^{-6}. \tag{34}$$

The results are consistent with both the PHENIX data and the results from an independent STAR analysis.

10.2 Nuclear modification factor R_{dAu}

To resolve if any modification of J/ψ production in $d + Au$ is presented due to the presence of nuclear matter, the nuclear modification factor was calculated

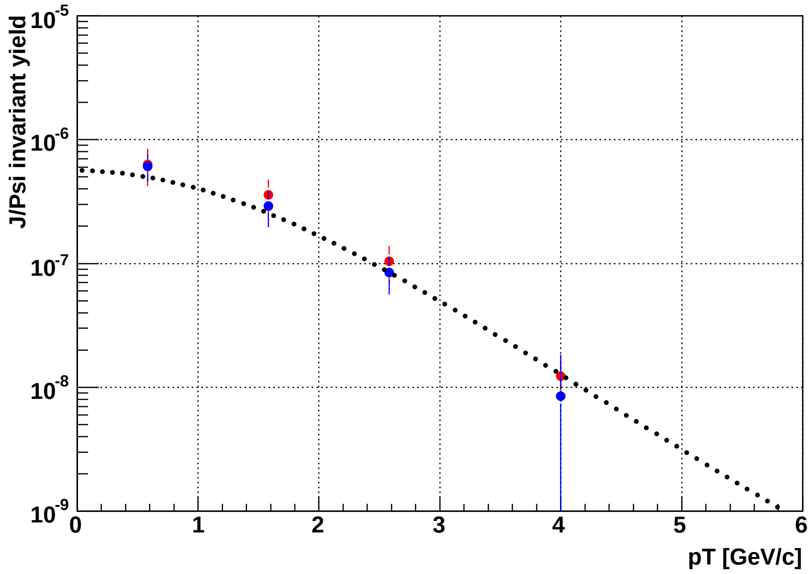

Figure 61: The corrected J/ψ p_T spectrum. Red marks show results obtained from this analysis, blue marks show results obtained from an independent analysis of same data sample [11], and the dotted line is a fit to the PHENIX data.

as

$$R_{dA} = \frac{\frac{dN_{dA}^{J/\psi}}{dy}}{< N_{coll} > \frac{dN_{pp}^{J/\psi}}{dy}}, \tag{35}$$

where the J/ψ yield in $p+p$ collision can be evaluated as

$$\frac{dN_{p+p}^{J/\psi}}{dy} = \frac{\sigma_{p+p}^{J/\psi}}{\sigma_{inel}}. \tag{36}$$

The inelastic cross section is $\sigma_{inel} = 42 \pm 3$ mb and the J/ψ cross section in $p+p$ collisions is $\sigma_{p+p}^{J/\psi} = 57 \pm 10\ (stat.) \pm 9\ (syst)$ nb [68]. The nuclear modification factor is shown in Fig. 62, where red marks show results obtained in this analysis, blue marks denote results from an independent analysis on same data, violet marks show results from PHENIX collaboration, and blue lines denote suppression predictions based on the modification of the PDF within the nucleus using EPS09 parametrization [54] [69]. The data obtained in this analysis are consistent with other results.

Centrality	$< N_{\rm coll} >$	$R_{dA}^{J/\psi}$
$0-20$	14.6	0.55 ± 0.18
$20-40$	10.9	0.48 ± 0.06
$40-100$	4.75	1.08 ± 0.13

Table 15: The nuclear modification factor R_{dA} for each centrality bin.

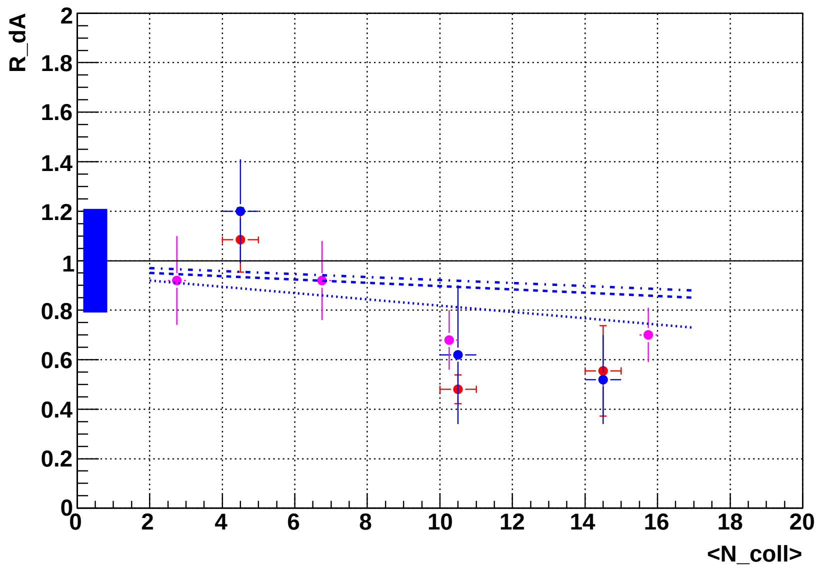

Figure 62: The J/ψ nuclear modification factor R_{dA} in $d+Au$ collisions. Red marks show results obtained in this analysis, blue marks denote results from an independent analysis of the same data, violet marks show results from PHENIX collaboration and blue lines denote suppression predictions based on the modification of the PDF within the nucleus using EPS09 parametrization [54] [69] for J/ψ absorption cross section of 0.0, 0.5 and 1.75 mb from the top to the bottom. The blue cube shows the normalization uncertainty of $p+p$ yield.

Conclusion

The J/ψ production in $d + Au$ collisions recorded during data taking in the year 2008 at STAR at RHIC was studied in the dielectron channel. Electrons and positrons were identified using the information from the TPC detector. Then the J/ψ reconstruction efficiency, included the detector acceptance and the track reconstruction efficiency was determined from reconstruction of Monte Carlo simulated J/ψs embedded into real events, and the electron identification efficiency was calculated by performing a multiple Gaussian fit to the dE/dx distribution in different p_T bins in real data. Total reconstruction efficiency is depending on p_T of J/Ψ and was determined to be between 10-25% in the measured region. The corrected spectrum was obtained.

Finally the invariant yield was obtained and compared with results from $p + p$ collisions at the same energy (2006). The nuclear modification factor was calculated as $R_{d+Au}^{J/\psi} = 0.55 \pm 0.18$ $(0.48 \pm 0.06, 1.08 \pm 0.13)$ for the most central, semi-peripheral, and peripheral collisions, respectively. The result was compared with other results from STAR and PHENIX collaborations and with models based on the modification of the PDF within the nucleus using EPS09 parametrization. These results are consistent with results from independent analysis published by STAR and PHENIX collaborations.

A List of invariant mass spectra for single p_T bins.

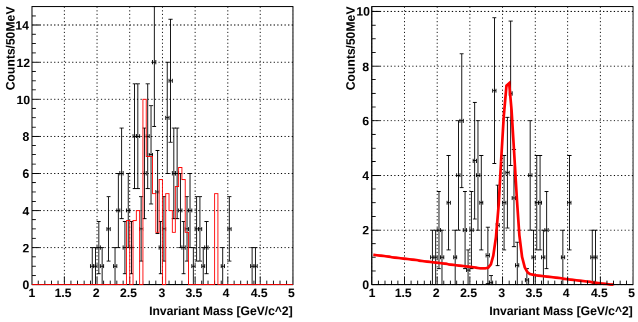

Figure 63: The uncorrected J/ψ invariant mass spectrum for all centrality and p_T bin 0-1 GeV.

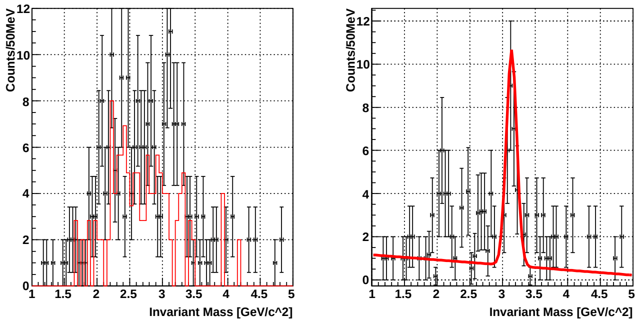

Figure 64: The uncorrected J/ψ invariant mass spectrum for all centrality and p_T bin 1-2 GeV.

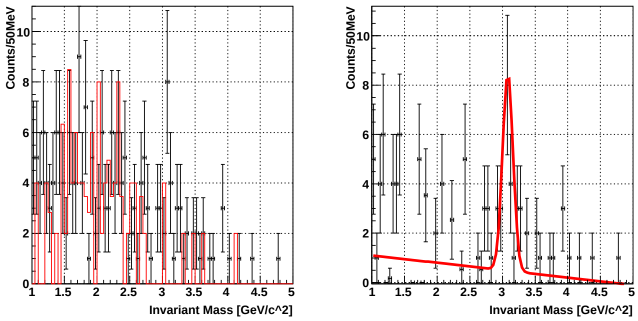

Figure 65: The uncorrected J/ψ invariant mass spectrum for all centrality and p_T bin 2-3 GeV.

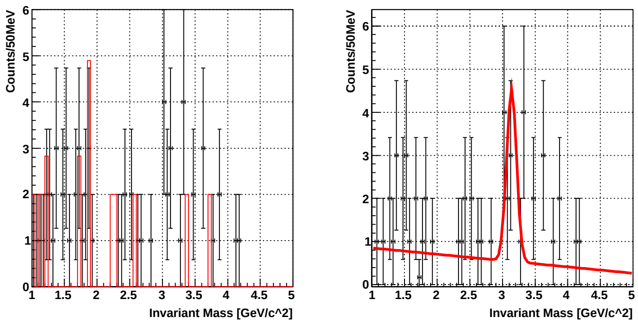

Figure 66: The uncorrected J/ψ invariant mass spectrum for all centrality and p_T bin 3-5 GeV.

B List of the dE/dx distributions for all p_T bins.

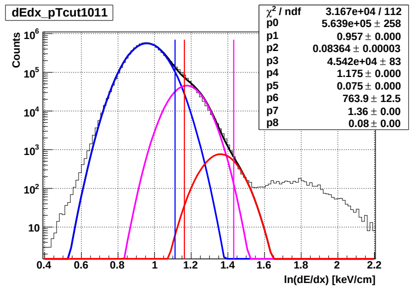

Figure 67: The dE/dx distribution for all charged particles that passed track quality cuts with $1.0 < p_T < 1.1$ GeV/c.

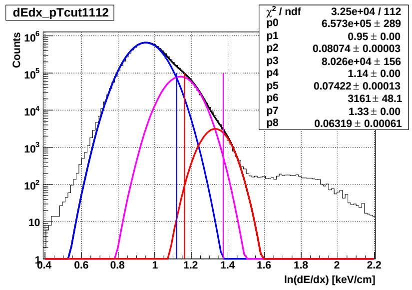

Figure 68: The dE/dx distribution for all charged particles that passed track quality cuts with $1.1 < p_T < 1.2$ GeV/c.

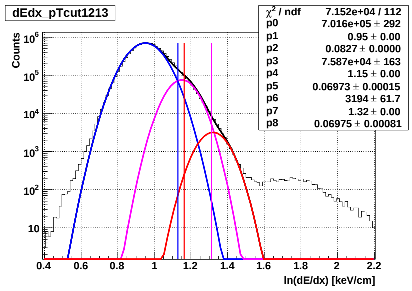

Figure 69: The dE/dx distribution for all charged particles that passed track quality cuts with $1.2 < p_T < 1.3$ GeV/c.

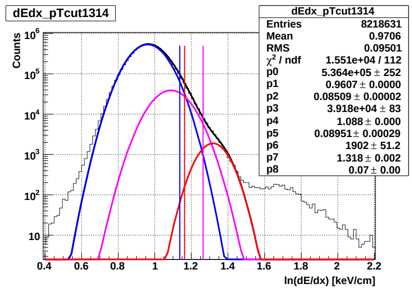

Figure 70: The dE/dx distribution for all charged particles that passed track quality cuts with $1.3 < p_T < 1.4$ GeV/c.

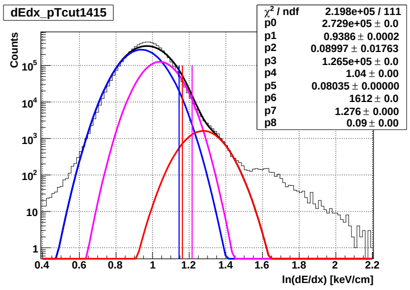

Figure 71: The dE/dx distribution for all charged particles that passed track quality cuts with $1.4 < p_T < 1.5$ GeV/c.

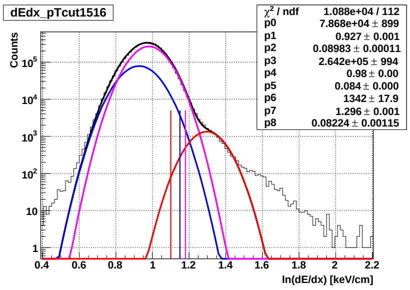

Figure 72: The dE/dx distribution for all charged particles that passed track quality cuts with $1.5 < p_T < 1.6$ GeV/c.

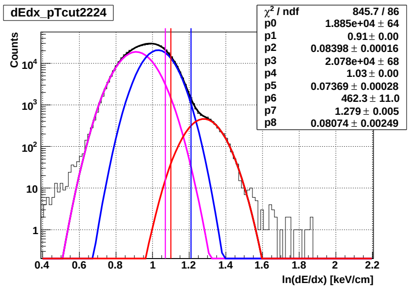

Figure 73: The dE/dx distribution for all charged particles that passed track quality cuts with $1.6 < p_T < 1.7$ GeV/c.

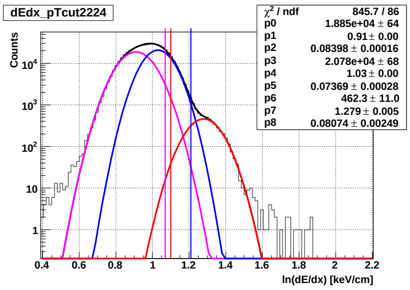

Figure 74: The dE/dx distribution for all charged particles that passed track quality cuts with $1.7 < p_T < 1.8$ GeV/c.

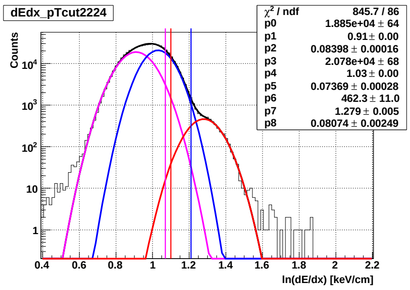

Figure 75: The dE/dx distribution for all charged particles that passed track quality cuts with $1.8 < p_T < 1.9$ GeV/c.

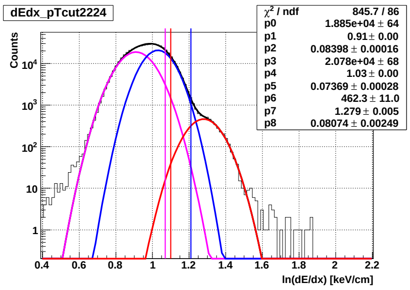

Figure 76: The dE/dx distribution for all charged particles that passed track quality cuts with $1.9 < p_T < 2.0$ GeV/c.

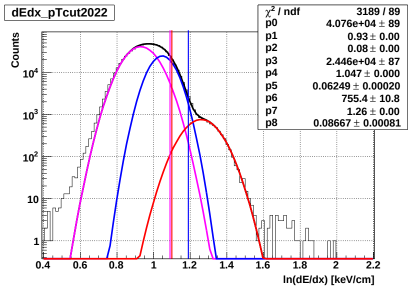

Figure 77: The dE/dx distribution for all charged particles that passed track quality cuts with $2.0 < p_T <$ 2.2 GeV/c.

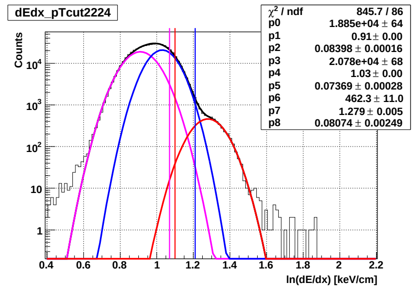

Figure 78: The dE/dx distribution for all charged particles that passed track quality cuts with $2.2 < p_T <$ 2.4 GeV/c.

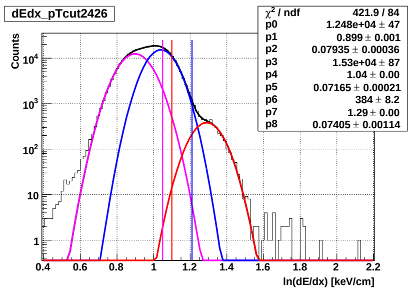

Figure 79: The dE/dx distribution for all charged particles that passed track quality cuts with $2.4 < p_T <$ 2.6 GeV/c.

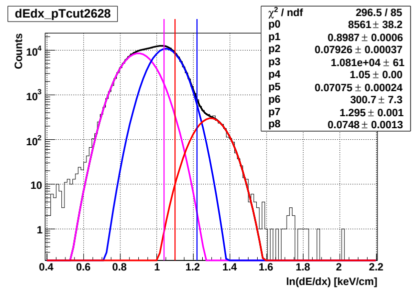

Figure 80: The dE/dx distribution for all charged particles that passed track quality cuts with $2.6 < p_T <$ 2.8 GeV/c.

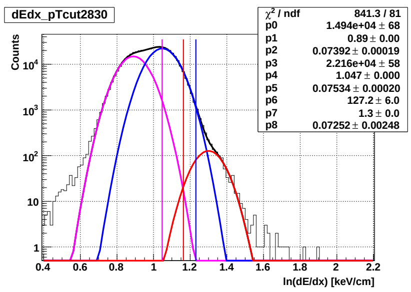

Figure 81: The dE/dx distribution for all charged particles that passed track quality cuts with $2.8 < p_T <$ 3.0 GeV/c.

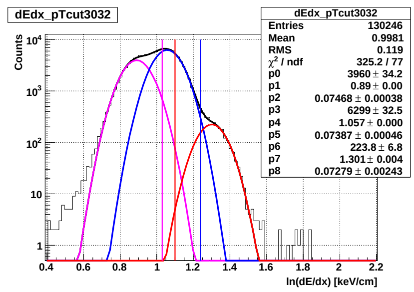

Figure 82: The dE/dx distribution for all charged particles that passed track quality cuts with $3.0 < p_T <$ 3.2 GeV/c.

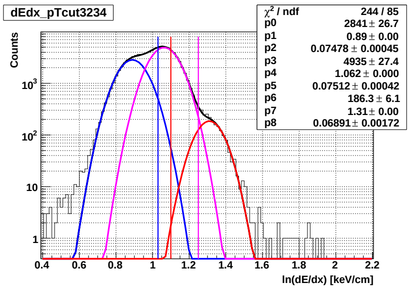

Figure 83: The dE/dx distribution for all charged particles that passed track quality cuts with $3.2 < p_T < 3.4$ GeV/c.

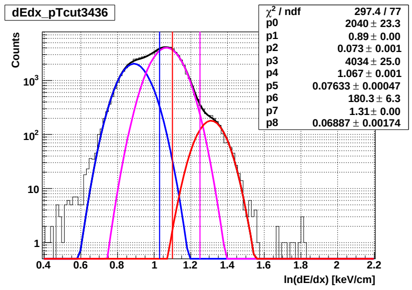

Figure 84: The dE/dx distribution for all charged particles that passed track quality cuts with $3.4 < p_T < 3.6$ GeV/c.

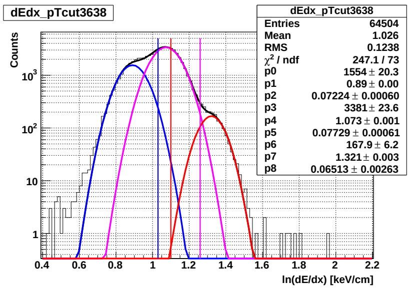

Figure 85: The dE/dx distribution for all charged particles that passed track quality cuts with $3.6 < p_T < 3.8$ GeV/c.

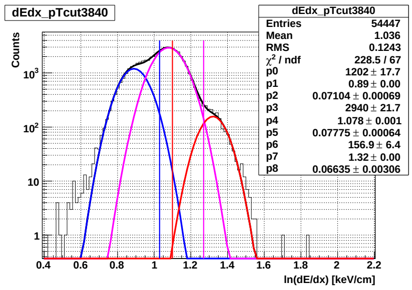

Figure 86: The dE/dx distribution for all charged particles that passed track quality cuts with $3.8 < p_T < 4.0$ GeV/c.

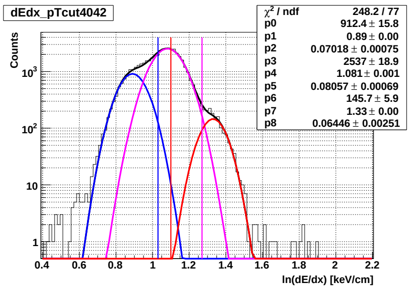

Figure 87: The dE/dx distribution for all charged particles that passed track quality cuts with $4.0 < p_T < 4.2$ GeV/c.

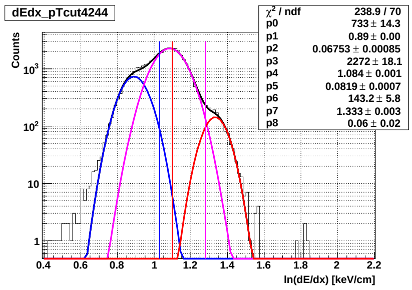

Figure 88: The dE/dx distribution for all charged particles that passed track quality cuts with $4.2 < p_T < 4.4$ GeV/c.

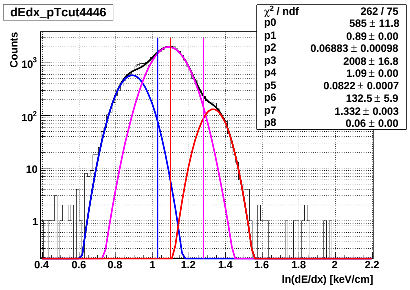

Figure 89: The dE/dx distribution for all charged particles that passed track quality cuts with $4.4 < p_T < 4.6$ GeV/c.

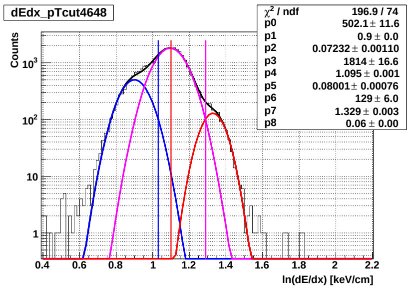

Figure 90: The dE/dx distribution for all charged particles that passed track quality cuts with $4.6 < p_T < 4.8$ GeV/c.

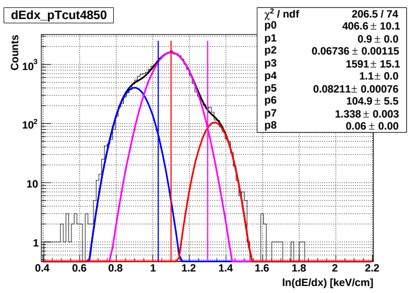

Figure 91: The dE/dx distribution for all charged particles that passed track quality cuts with $4.8 < p_T < 5.0$ GeV/c.

C List of presentations and publications

List of presentations

1 Low p_T J/ψ production in $d+Au$ collisions, STAR Collaboration meeting, Juniors Afternoon Session 2009

2 Low p_T J/ψ in $d+Au$, STAR Collaboration meeting, Heavy Flavor Physics Working Group Parallel Session 2009

3 J/ψ measurements in $d+Au$ at STAR, IDPACS Sesimbra Portugal 2011

4 Rekonstrukce J/ψ mezonů ve srážkách $d+Au$ na experimentu STAR, Workshop EJF 2011

5 Rekonstrukce J/ψ mezonů ve srážkách $d+Au$ na experimentu STAR, CFRJS 2011

6 J/ψ measurements at STAR (for STAR Collaboration), SVK Ostrava 2011

7 J/ψ measurements at STAR, STAR Collaboration meeting (student day) 2011

List of publications

1 H.Agakishiev et al. (STAR Collaboration), Observation of the antimatter helium-4 nucleus. arXiv:1103.3312 (2011)

2 H.Agakishiev et al. (STAR Collaboration), High pT non-photonic electron production in p+p collisions at $\sqrt{s_{nn}} = 200$ GeV., Phys.Rev. D83 (2011) 052006 (2011)

3 H.Agakishiev et al. (STAR Collaboration), Studies of di-jet survival and surface emission bias in $Au + Au$ collisions via angular correlations with respect to back-to-back leading hadrons., arXiv:1102.2669 (2011)

4 H.Agakishiev et al. (STAR Collaboration), Measurements of Dihadron Correlations Relative to the Event Plane in $Au+Au$ Collisions at $\sqrt{s_{nn}} =$ 200 GeV., arXiv:1010.0690 (2010)

5 M.M. Aggarwal et al. (STAR Collaboration), Strange and Multi-strange Particle Production in Au+Au Collisions at $\sqrt{s_{nn}} = 62.4$ GeV., Phys.Rev. C83 024901 (2011)

References

[1] T.Matsui, H.Satz, J/ψ Suppresion by Quark Gluon Plasma, Physics Letters B, vol.178, no.4 (1986)

[2] K. Nakamura et al., Particle Data Group, J. Phys. G 37, 075021 (2010)

[3] M. Vlasák, Influence of Pile-up on the Search for Black Hole at LHC, diploma thesis (2011)

[4] R. Vogt, Ultrarelativistic heavy-ion collisions, Lawrence Berkeley laboratory (2007)

[5] P. Petreczkya, QCD Thermodynamics on lattice, Nucl. Phys. B140, 78 (2004)

[6] J. B. Kogout, The lattice gauge theory approach to quantum chromodynamics, Rev. Mod. Phys. 55, 775 (1983)

[7] S. Oda, Production of Charmonia in Cu+Cu and p+p Collisions at $\sqrt{s}$=200 GeV, Dissertation thesis (2008)

[8] G. Taku, J/ψ Production in High Energy Heavy Ion Collisions at RHIC, Dissertation thesis (2007)

[9] J. D. Bjorken, Highly relativistic nucleus-nucleus collisions: The central rapidity region, Phys. Rev. D 27, 140 (1983)

[10] R. J. Glauber, Lectures on Theoretical Physics , Interscience, New York, Vol. I. (1959)

[11] Christopher Powell (STAR Collaboration), J/ψ Production in d+Au collisions at $\sqrt{s_{nn}} = 200$ GeV at the STAR Experiment (2010)

[12] A. Dainese, Review on Heavy-Ion Physics, arXiv:1012.4038v1 (2010)

[13] S. Sarkar, H. Satz, B. Sinha, The Physics of the Quark-Gluon Plasma, Springer (2010)

[14] R. Bayer, R. Rückl, Z. Phys. C19 251 (1983)

[15] G. T. Bodwin, E. Braaten, G.P.Lepage, Rigorous QCD analysis of inclusive annihilation and production of heavy quarkonium, Phys. Rev. D 51 1125 (1995)

[16] M. B. Einhorn, S. D. Ellis, Heavy-quark content of light hadrons and implications for the γ-family, Phys. ev. D12 (1975)

[17] P.Hoyer, S. Peigne, Quarkonium production through hard comover scattering, Phys. Rev. D59 (1999)

[18] H. Satz, X. N. Wang, Hard Processes in Hadronic Interactions, Int. J. Mod. Phys. A 10, 2881 (1995)

[19] M. Mangano et al., Hard Probes in Heavy-Ion Collisions at the LHC, CERN Yellow Report 2004–09, Geneva (2004)

[20] N. Brambilla, M. Krämer, R. Mussa, A. Vairo, Heavy quarkonium physics, CERN (2005)

[21] F. Abe et al., J/ψ and ψ(2S) Production in pp Collisions at $\sqrt{s_{NN}} = 1.8$ TeV, Phys. Rev. Lett. 79, 572 (1997)

[22] A. Abulencia et al., Polarizations of J/ψ and $\Upsilon(2S)$ Mesons Produced in $p\bar{p}$ Collisions at $\sqrt{s_{NN}} = 1.96$ TeV, Phys. Rev. Lett. 99, 132001 (2007).

[23] N. Brambilla et al., Heavy quarkonium: progress, puzzles, and opportunities, The European Phys. Jour. C, Vol 71, No. 2, (2010)

[24] P. Faccioli, C. Laurenc, J. Seixas, High Energy Phys. 10, 004 (2008) 201, 202

[25] B. I. Abelev et al. (STAR Collaboration), J/ψ production at high transverse momenta in p+p and Cu+Cu collisions at $\sqrt{s_{NN}} = 200$ GeV, Phys. Rev. C 80, 041902 (2009)

[26] Helmut Satz, Colour Deconfinement and J/ψ Suppression in High Energy Nuclear Collisions, BI-TP 97/47, hep-ph/9711289v1 (2007)

[27] S. Digal, P. Petreczky and H. Satz, Quarkonium feed-down and sequential suppression, Phys. Rev. D 64, 094015 (2001)

[28] G. Ropke, D. Blaschke and H. Schulz, Dissociation kinetics and momentum-dependent J/ψ suppression in a quark-gluon plasma, Phys. Rev. D 38 (1988) 3589.

[29] F. Karsch, M. T. Mehr and H. Satz, Color screening and deconfinement for bound states of heavy quarks, Z. Phys. C 37 (1988) 617.

[30] T. Hashimoto, K. Hirose, T. Kanki and O. Miyamura, The Dissipative Potential Induced by QCD at Finite Temperature and Density, Z. Phys. C 38 (1988) 251

[31] T. Umeda, K. Nomura and H. Matsufuru, Charmonium at finite temperature in quenched lattice QCD, Eur. Phys. J. C39 S1 (2005)

[32] S. Datta, F. Karsch, P. Petreczky and I. Wetzorke, A Study of Charmonium Systems across the Deconfinement Transition, arXiv:hep-lat/0208012

[33] J.D. Bjorken, J.G. Korner et al., Lecture Notes in Physics, Vol. 56 (1976)

[34] L. Grandchamp, R. Rapp and G. E. Brown, In-Medium Effects on Charmonium Production in Heavy-Ion Collisions, Phys. Rev. Lett. 92 (2004)

[35] L. Yan, P. Zhuang, Nu. Xu, J/ψ Production in Quark-Gluon Plasma, Phys. Rev. Lett. 97 232301 (2006)

[36] P. Braun-Munzinger, I. Heppe and J. Stachel, Chemical equilibration in Pb+Pb collisions at the SPS, Phys. Lett. B465 (1999)

[37] E. L. Bratkovskaya, A. P. Kostyuk, et al., Transverse Pressure in Relativistic Nuclear Collisions: Evidence for Partonic Interactions?, Phys. Rev. C 69 (2004)

[38] O. Linnyk E. L. Bratkovskaya, W. Cassing, Open and Hidden Charm in proton-nucleus and heavy ion colisions, Int. J. Mod. Phys. E17 1367-1439 (2008)

[39] L. Bravina, K. Tywoniuk, et al., Resolving the J/ψ RHIC puzzles at LHC, Phys. G36 064054 (2009)

[40] Aleksi Kurkela, Paul Romatschke, Aleksi Vuorinen, Cold Quark Matter, Phys. Rev. D 81 105021 (2010)

[41] N. Armesto, Nuclear shadowing, J. Phys. G32 R367-R394 (2006)

[42] Wei Zhu, Jianhong Ruan, and Fengyao Hou, From EMC effect to Cronin effect, arXiv:1012.4224v1 (2010)

[43] A. R. Timmins (STAR Collaboration), Strange Particle Production at RHIC, Eur. Phys. J. C62 (2009)

[44] M. Gyulassy, X. Wang, Nucl. Phys. B420, 583 (1994)

[45] C. Alder et al. (STAR Collaboration), Disappearance of back-to-back high p_T hadron correlations in central Au+Au collisions at $\sqrt{s_{NN}}$ = 200-GeV, Phys. Rev. Lett. 90, 082302 (2003)

[46] S. Soff, Strangeness Enhancement in Heavy Ion Collisions - Evidence for Quark- Gluon-Matter, Phys. Lett. B471, 89 (1999)

[47] D. d'Enterria, Jet quenching, arXiv:0902.2011v2 [nucl-ex]

[48] B. Mohanty, QCD Phase Diagram: Phase Transition, Critical Point and Fluctuations, arXiv:0907.4476v3 [nucl-ex] (2009)

[49] V. Tram, F. Arleo, Global analysis of J/ψ suppression in cold nuclear matter, Eur. Phys. J. C61, 847 (2009)

[50] A. Adare et al., Cold Nuclear Matter Effects on J/ψ Production as Constrained by Deuteron-Gold Measurements at $\sqrt{s_{NN}} = 200$ GeV, Phys. Rev. C 77 024912 (2008)

[51] O. Hajkova (STAR Collaboration), J/ψ Measurements at STAR, SVK Ostrava (2011)

[52] A. Adare et al., J/ψ $\sqrt{s_{NN}} = 200$ GeV Cu + Cu Collisions, Phys. Rev. Lett. 101, 122301 (2008)

[53] A. Adare et al.,J/ψ Production versus Centrality, Transverse Momentum, and Rapidity in Au+Au Collisions at $\sqrt{s_{NN}} = 200$ GeV, Phys. Rev. Lett. 98, 232301 (2007)

[54] Christopher Powell (STAR Collaboration), Low-pT J/ψ Production in d+Au Collisions at $\sqrt{s_{NN}} = 200$ GeV in STAR (2011)

[55] J.Wolf et al. (STAR Collaboration), STAR detector overview (2003)

[56] M. Harisson et al., RHIC project overview, Nucl. Instr. and Meth. A 499 235 (2003)

[57] M. Anderson et al. (STAR Collaboration), The STAR Time Projection Chamber: A Unique Tool for Studying High Multiplicity Events at RHIC, Nucl. Instrum. Meth. A499 (2003)

[58] P. Fachini, Zhangbu Xu et al. (STAR TOF Collaboration), Proposal for a Large Area Time of Flight System for STAR, STAR TOF Proposal (2004)

[59] K.H. Ackermann et al. (STAR Collaboration), The Forward Time Projection Chamber (FTPC) in STAR, Nucl. Instrum. Meth. A499 (2003)

[60] M. Sharma, A Study of Fluctuations in Ultra-Relativistic Heavy Ion Collisions, Dissertation thesis (2008)

[61] Hans Bichsel (STAR Collaboration), Particle identification at STAR-TPC with ionization measurements (2003)

[62] Ming Shao, Olga Barannikova et al. (STAR Collaboration), Extensive Particle Identification with TPC and TOF at the STAR Experiment, Nucl. Instrum. Meth. A558 (2006)

[63] M.Beddo et al. (STAR Collaboration), The STAR Barrel Electromagnetic Calorimeter (2002)

[64] M. Calderon et al., Extending the physics reach of star: Prospects for the measurement of quarkonia., Tech. rep. (2003)

[65] Daniel Kikola (STAR Collaboration), Hidden charm production in the relativistic heavy ion collisions registered in the STAR experiment, Dissertation thesis (2010)

[66] Stephen Baumgart (STAR Collaboration), J/ψ production at high transverse momentum in p+p and A+A collisions, disertation thesis (2009)

[67] Ming Shao et al. (STAR Collaboration), Extensive particle identification with TPC and TOF at the STAR experiment, disertation thesis (2006)

[68] M. Cosentino (STAR Collaboration), J/ψ production in $p+p$ collisions at $\sqrt{s_{NN}} = 200$ GeV in the STAR experiment, arXiv:0806.0347 (2008)

[69] K.J. Eskola et al., JHEP04, 065 (2009)